ORCA – Online Research @ Cardiff

This is an Open Access document downloaded from ORCA, Cardiff University's institutional repository:https://orca.cardiff.ac.uk/id/eprint/167097/

This is the author's version of a work that was submitted to / accepted for publication.

Citation for final published version:

Luangwanta, Tawanwit, Chachvalvutikul, Auttaphon and Kaowphong, Sulawan 2024. Enhanced visible-light photocatalytic activity of FeVO4/Bi2WO6 heterojunction via Z-scheme charge-transfer mechanism. Materials Research Bulletin 170 , 112560. 10.1016/j.materresbull.2023.112560

Publishers page: http://dx.doi.org/10.1016/j.materresbull.2023.1125...

Please note:
Changes made as a result of publishing processes such as copy-editing, formatting and page numbers may not be reflected in this version. For the definitive version of this publication, please refer to the published source. You are advised to consult the publisher's version if you wish to cite this paper.

This version is being made available in accordance with publisher policies. See http://orca.cf.ac.uk/policies.html for usage policies. Copyright and moral rights for publications made available in ORCA are retained by the copyright holders.

Enhanced visible-light photocatalytic activity of $FeVO_4/Bi_2WO_6$ heterojunction via Z-scheme charge-transfer mechanism

Tawanwit Luangwanta[a], Auttaphon Chachvalvutikul[a], Sulawan Kaowphong[a,b,c]*

[a] Department of Chemistry, Faculty of Science, Chiang Mai University, Chiang Mai 50200, Thailand

[b] Center of Excellence in Materials Science and Technology, Chiang Mai University, Chiang Mai 50200, Thailand

[c] Materials Science Research Center, Faculty of Science, Chiang Mai University, Chiang Mai 50200, Thailand

* Corresponding author

E–mail address: sulawank@gmail.com

Tel: +66 53 943341 Fax: +66 53 892277

Abstract

The design and construction of a Z-scheme heterojunction, aiming to strengthen its redox ability for photocatalytic applications, is challenging. In this study, **a series of x mol%-$FeVO_4/Bi_2WO_6$ heterostructures** were fabricated. **$FeVO_4$ content was tuned for enhanced organic pollutants photodegradation. The 2.5 mol%-$FeVO_4/Bi_2WO_6$ photocatalyst exhibited superior photodegradation efficiency with high recyclability and stability for bisphenol A and methylene blue, which was 3.3 and 2.6 times faster than that of Bi_2WO_6, respectively. Moreover, the fabricated photocatalyst showed remarkable selectivity toward methylene blue as compared to that toward brilliant green and methyl orange.** The photo-efficacy was enhanced owing to the close interfacial contact between Bi_2WO_6 and $FeVO_4$ nanoparticles, resulting in a Z-scheme $FeVO_4/Bi_2WO_6$ heterojunction, which enabled efficient charge transfer imparting strong reducing ability to the electrons for the reduction of O_2 to $\bullet O_2^-$, and subsequent production of H_2O_2 and •OH. This work highlights a potential photocatalyst for photodegradation of environmental pollutants.

KEYWORDS: $FeVO_4/Bi_2WO_6$, Nanocomposite, Z-scheme, Heterostructure, Photodegradation

1. Introduction

In recent years, water pollution has become a major environmental threat with detrimental effects on humans and other living organisms. The treatment of organic pollutants in wastewater is particularly challenging owing to their complex chemical structures and toxicity. However, photocatalysis has emerged as a promising technology that utilizes renewable energy sources and photocatalysts to treat wastewater owing to its several advantages, such as complete mineralization, no waste disposal problems, low cost, and mild

reaction conditions [1,2]. Conventionally, metal oxide semiconductors, such as TiO_2, ZnO, and SnO_2, have been commercially used as photocatalysts for wastewater purification because of their high chemical stability, low toxicity, low cost, and high availability [3]. However, wide bandgaps of TiO_2 (3.2 eV), ZnO (3.3 eV), and SnO_2 (3.6 eV) are limited to the ultraviolet (UV) region, which accounts for only 5% of the solar spectrum. To effectively utilize sunlight, considerable efforts have been made for developing new visible-light-active semiconductor photocatalysts [4,5].

Recently, Bi_2WO_6 has gained substantial attention for its potential use in a wide range of photocatalytic applications, owing to its moderate bandgap (2.7 eV), high thermal and chemical stabilities, strong oxidizing ability, and high photoactivity [6,7]. The valence band (VB) of Bi_2WO_6 is composed of O 2*p* and Bi 6*s* hybrid orbitals, whereas those of metal oxides generally consist of only O 2*p* orbitals. The overlap of O 2*p* and Bi 6*s* orbitals in the VB of Bi_2WO_6 increases the mobility of photogenerated charges, thus improving the photocatalytic activity [8,9]. Moreover, a special layered structure comprising the corner-sharing WO_6 octahedra sandwiched between $(Bi_2O_2)^{2+}$ slices facilitates the separation of photogenerated electron $(e)^-$/hole (h^+) pairs, which can effectively migrate to the Bi_2WO_6 surface [10,11]. However, the practical applications of Bi_2WO_6 are limited by the rapid recombination rate of the photogenerated e^-/h^+ pairs, which reduces the quantum efficiency of photocatalysis [12].

The heterojunction photocatalyst strategy is a promising approach to enhance the photocatalytic efficiency of materials by promoting the separation of photogenerated e^-/h^+ pairs, reducing their recombination, and extending the light absorption range. Additionally, this strategy offers improved stability and durability of the photocatalyst [13–15]. Therefore, designing and fabricating novel Bi_2WO_6-based heterojunctions with better visible-light utilization and efficient charge separation efficiency for boosting photocatalytic performances have been extensively investigated up to date [16–25]. The

selection of guest/host components depends on the band structure alignment between the chosen components, the specific applications, and desired photocatalytic performance [19,26]. The incorporation of Bi_2WO_6 with metal–organic frameworks (MOFs) such as MIL-101(Fe) and Bi-MOF exhibited an improved visible-light driven photocatalytic performance for antibiotic degradation and Cr(VI) reduction [17,18]. Additionally, the combination of Bi_2WO_6 with other semiconductor materials having appropriately matched band structures can be utilized to form semiconductor-semiconductor heterojunctions, such as $Bi_2WO_6/ZnIn_2S_4$ [16], Sb_2WO_6/Bi_2WO_6 [19], TiO_2-Bi_2WO_6 [20], α-Fe_2O_3/Bi_2WO_6 [21], $Cd_{0.5}Zn_{0.5}S/Bi_2WO_6$ [22], $Cd_{0.5}Zn_{0.5}S$/carbon dots/Bi_2WO_6 [23], TaON/Bi_2WO_6 [24], and Ag_3PO_4/Bi_2WO_6 [25], which can promote the separation and migration of photogenerated charges, thus resulting in enhanced photocatalytic performance.

$FeVO_4$ has a narrow bandgap (2.05 eV) and shows visible-light absorption, starting at approximately 600 nm, which enables solar energy harvesting in the visible-light region [27,28]. Nanocrystalline $FeVO_4$ is a highly stable and selective catalyst for photocatalytic CO_2 reduction [27], photocatalytic degradation of organic pollutants [29,30], and catalytic dehydrogenation [31]. We previously reported that $FeVO_4$ nanoparticles coupled with bismuth-based photocatalysts, such as $Bi_7O_9I_3$ [32], BiOCl [33], $Bi_4O_5Br_2$ [34], and $Bi_4O_5Br_2$/BiOBr [35] exhibited significantly increased visible-light-driven photocatalytic degradation with high stability against photo- and chemical corrosion. Consequently, $FeVO_4$ was selected and coupled with Bi_2WO_6 to improve the photogenerated charge separation efficiency. Moreover, the valence band (VB) and conduction band (CB) potentials of $FeVO_4$ and Bi_2WO_6 match well, resulting in the $FeVO_4/Bi_2WO_6$ heterojunction with a staggered band structure [16,34]. These phenomena are beneficial for efficient interfacial charge transfer that spatially separates the charge carriers and reduces the rate of e^-/h^+ pair recombination, thereby improving

photocatalytic activity. To the best of our knowledge, there have been no reports on the fabrication of $FeVO_4/Bi_2WO_6$ heterojunction photocatalysts or their degradation of organic pollutants.

In this study, Bi_2WO_6 and $FeVO_4$ nanoparticles were fabricated using the microwave irradiation method, followed by calcination. Microwave irradiation offers rapid volumetric heating, which accelerates the rate of chemical reactions, resulting in the formation of nanostructured materials in a short reaction time as compared to those using conventional heating methods [36]. A series of x mol%-$FeVO_4/Bi_2WO_6$ nanocomposites were prepared using a modified wet impregnation method. The photocatalytic degradation of bisphenol A (BPA) and methylene blue (MB), which are the models for non-dye and dye organic pollutants, respectively, were evaluated under visible-light irradiation. Further, the photodegradation efficiencies of brilliant green (BG) and methyl orange (MO) were investigated to evaluate the selectivity of the photocatalyst for organic dye pollutants. The band alignment of the $FeVO_4/Bi_2WO_6$ heterojunction and the Z-scheme charge-transfer pathway were proposed based on a comprehensive analysis of the optical characterizations, energy band positions, active species scavenging experiments, **electron spin resonance measurements**, and the reduction potentials of the reactive oxygen species.

2. Experimental procedure

2.1. Preparation of Bi_2WO_6, $FeVO_4$, and $FeVO_4/Bi_2WO_6$

For the Bi_2WO_6 preparation, $Bi(NO_3)_3 \cdot 5H_2O$ and $Na_2WO_4 \cdot 2H_2O$ (2:1 molar ratio) were separately dissolved in deionized water (20.0 mL) and then mixed under magnetic stirring (30 min). **Subsequently, the mixed solution was transferred into a glass flask with a 250.0 mL capacity. The flask was unsealed and irradiated using 2.45 GHz microwave radiation operating at 600 W for 30 cycles.** The microwave power was turned on for 30 s and off for

60 s in each cycle. Finally, the obtained powder was filtered, washed several times with deionized water and ethanol, and dried overnight in an oven at 70 °C. The as-prepared powders were calcined at 500 °C for 5 h at a heating rate of 5 °C/min.

For the $FeVO_4$ preparation, $Fe(NO_3)_3.9H_2O$ and NH_4VO_3 (1:1 molar ratio) were separately dissolved in deionized water (20.0 mL) and mixed under magnetic stirring (30 min). Subsequently, the pH value of the mixed solution was adjusted to 4 by slowly adding 2.0 M NH_4OH solution. Thereafter, the solution was mechanically stirred for 30 min, and subsequently, the mixed solution was transferred to the unsealed glass flask and irradiated under 600 W of microwave radiation for 30 cycles, followed by calcination at 600 °C for 5 h at a heating rate of 5 °C/min.

The $FeVO_4/Bi_2WO_6$ nanocomposites were fabricated using the modified wet impregnation method [32]. An appropriate amount of the $FeVO_4$ powder was dispersed in methanol (40.0 mL) under sonication for 30 min. Subsequently, the required amount of Bi_2WO_6 powder was added to the dispersion. Then, the suspension was mechanically stirred for 24 h to completely evaporate the residual methanol. Finally, the resulting $FeVO_4/Bi_2WO_6$ powder was dried at 70 °C, followed by heat treatment at 200 °C for 30 min. The $FeVO_4$ contents in the $FeVO_4/Bi_2WO_6$ nanocomposites were varied at 1.25, 2.5, 5, and 10 mol%. For comparison, a physical mixture of $FeVO_4$ and Bi_2WO_6 was prepared via physical grinding, designated as P2.5 mol%-$FeVO_4/Bi_2WO_6$.

2.2. Materials characterizations and electrochemical studies

X-ray diffraction (XRD) patterns of the synthesized powders were recorded using an X-ray diffractometer (Rigaku Smartlab). The morphology and particle size of the powders were investigated using transmission electron microscopy (TEM, JEOL JEM-2010) and field emission scanning electron microscopy (FESEM, JEOL JSM-6335F) with energy dispersive

X-ray (EDX) spectroscopy. **Chemical state and elemental composition were determined via X-ray photoelectron spectroscopy (XPS, AXIS ultra DLD, Kratos Analytical Ltd.) using an Al Kα X-ray source at 1.4 keV radiation.** The optical properties were studied using UV–vis diffuse reflectance spectroscopy (UV–vis DRS, UV-1800 Shimadzu) and photoluminescence spectroscopy (PL, AvaSpec-2048TEC-USB2 Avantes) at an excitation wavelength of 345 nm. **The specific surface area and total pore volume of the samples were investigated via N_2 adsorption at -196 °C using a Quantachrome instrument and calculated using the Brunauer-Emmett-Teller (BET) and Barrett-Joyner-Halenda (BJH) methods, respectively. Before the analysis, the samples were degassed at 120 °C for 3 h under vacuum.**

The pH at the potential of zero point charge (pH_{PZC}) of the photocatalyst was determined based on the pH drift method [37]. Briefly, 200 mL of deionized water with an initial pH of 3–10 was prepared using 1 M HCl and 1 M NaOH. The photocatalyst (100 mg) was added to the solution and stirred continuously for 24 h. Thereafter, the final pH of the solution was measured, and the relationship between the initial and final pH was studied.

The electrochemical properties were investigated using an electrochemical analyzer (Metrohm Autolab potentiostat/galvanostat, PGSTAT128N) equipped with a standard three-electrode system with Ag/AgCl (3.0 M KCl) as the reference electrode, a platinum wire as the counter electrode, and a sample film with a fixed area of 1 cm^2 on the fluorine-doped tin-oxide-coated glass as the working electrode. For the electrolyte, 0.5 M Na_2SO_4 (pH 6) was used. Electrochemical impedance spectroscopy (EIS) was performed in the frequency range of 10^5–10^{-1} Hz with an amplitude of 0.05 V at a bias potential of 1.50 V in the dark. Mott–Schottky plots were recorded at a frequency of 10 Hz without an external bias.

2.3. Photocatalytic experiments

The photocatalytic activity was evaluated via the degradation of colorless BPA and organic dyes (MB, BG, and MO). The photocatalyst (100 mg) was dispersed in 200 mL of an aqueous solution of the target organic pollutant (2×10^{-5} mol L^{-1}) and the suspension was magnetically stirred in the dark for 30 min to establish an adsorption–desorption equilibrium on the surface of the photocatalyst. **Subsequently**, the suspension was exposed to 50 W LED light **with a vertical distance of 10 cm between the LED lamp and the horizontal surface of the suspension (Fig. S1). The suspension was continuously stirred magnetically during the light irradiation.** Every 30 min, the suspension (2.5 mL) was sampled, and the photocatalyst powder was separated via centrifugation. The concentrations of the remaining solutions were determined using a UV–vis spectrophotometer at maximum absorption wavelengths (λ_{max}) of 276, 664, 464, and 624 nm for BPA, MB, MO, and BG, respectively. Photolysis of these organic pollutants (blank experiment) was performed under the same experimental conditions. The photodegradation efficiency (%DE) and apparent rate constant (k, min^{-1}) for the degradation of organic pollutants were calculated using the equations (1) and (2):

$$\%DE = \frac{C_0 - Ct}{C_0} x100 \qquad (1)$$

$$\ln\left(\frac{C_0}{C_t}\right) = kt \qquad (2)$$

where C_0 and C_t represent the concentrations of the targeted organic pollutant after the photocatalyst surface reaches adsorption–desorption equilibrium and light irradiation, respectively, and t represents the reaction time (min). **Total organic carbon (TOC) concentration in the supernatant solution was measured using a TOC analyzer (Muti N/C 3100, Analytik Jena AG, Germany).**

To determine the reactive species in the photocatalytic reaction, the reactive-species scavenging experiments were carried out by adding 1×10^{-3} mol L^{-1} of dimethyl sulfoxide (DMSO) or isopropanol (IPA), *p*-benzoquinone (BQ), ammonium oxalate (AO), and $AgNO_3$ to the reaction systems to trap hydroxyl radicals (•OH), superoxide radicals ($•O_2^-$), h^+, and e^-, respectively. **The electron spin resonance (ESR) signal of the radicals, spin-trapped by 5,5-dimethyl-l-pyrroline-N-oxide (DMPO) was determined on a Bruker EMXmicro spectrometer. The ESR signals for liquid samples were recorded with an X-band frequency of 9.870 GHz and a field modulation of 100 kHz.** Ag and PbO_2 photodeposition experiments were further conducted to demonstrate the charge-transfer process in the $FeVO_4/Bi_2WO_6$ heterojunction. The photocatalyst (20 mg) was added to 100 mL of a 1×10^{-3} mol L^{-1} $AgNO_3$ solution (or $Pb(NO_3)_2$ solution). The reactions were irradiated with a 50 W LED light for 330 min. Thereafter, the photocatalyst powders were filtered, washed several times with deionized water and ethanol, and dried in an oven at 70 °C overnight. Finally, the photocatalyst powders after the photodeposition of Ag and PbO_2 nanoparticles were investigated using TEM.

3. Results and discussion

3.1. Structural and morphological studies

The XRD patterns of the Bi_2WO_6 and $FeVO_4$ samples, **prepared under microwave radiation, and the corresponding calcined samples** are shown in **Fig. S2**. **The XRD spectrum of the as-prepared Bi_2WO_6 sample (Fig. S2(a)) exhibits orthorhombic Bi_2WO_6 (JCPDS No. 00-039-0256) and tetragonal $Bi_{14}W_2O_{27}$ (JCPDS No. 00-039-0061) crystal phases. After calcination (Fig. S2(c)), a single phase of Bi_2WO_6 is detected, indicating that Bi_2WO_6 is successfully synthesized via the microwave irradiation method and subsequent calcination. For the as-prepared $FeVO_4$ sample (Fig. S2(b)), the pure phase of $FeVO_4$ with**

a tetragonal structure (JCPDS No. 00-038-1372) is detected without characteristic peaks of other impurities, indicating the high purity of the $FeVO_4$ sample obtained via microwave irradiation method. After calcination (Fig. S2(d)), the intensity of the diffraction peak becomes stronger, implying an improved degree of crystallinity. The XRD patterns of all the $FeVO_4/Bi_2WO_6$ nanocomposites (**Fig. 1** and **Fig. S3**) display no diffraction signals corresponding to $FeVO_4$ even with an increase in loading content to 10 mol%. This could be attributed to the substantially lower content of $FeVO_4$ in the nanocomposites and the relatively strong diffraction signal of the Bi_2WO_6 powder (**Fig. S2**(c and d)). **Furthermore, the positions of the diffraction peaks of Bi_2WO_6 and $FeVO_4$ in the nanocomposites did not shift when compared with that of pure Bi_2WO_6 and $FeVO_4$, suggesting that the combination of Bi_2WO_6 and $FeVO_4$ does not affect their crystal structures. Although the diffraction peak intensity of all the nanocomposites is nearly identical, the degree of crystallinity of all the nanocomposites (provided in Fig. S3), calculated based on the integration method, slightly decreases when compared to that of pure Bi_2WO_6. This implies that the combination of the two materials results in an interaction at the contact interface [20].** The coexistence of $FeVO_4$ in the $FeVO_4/Bi_2WO_6$ nanocomposite was further confirmed using TEM, **XPS**, and UV–vis DRS.

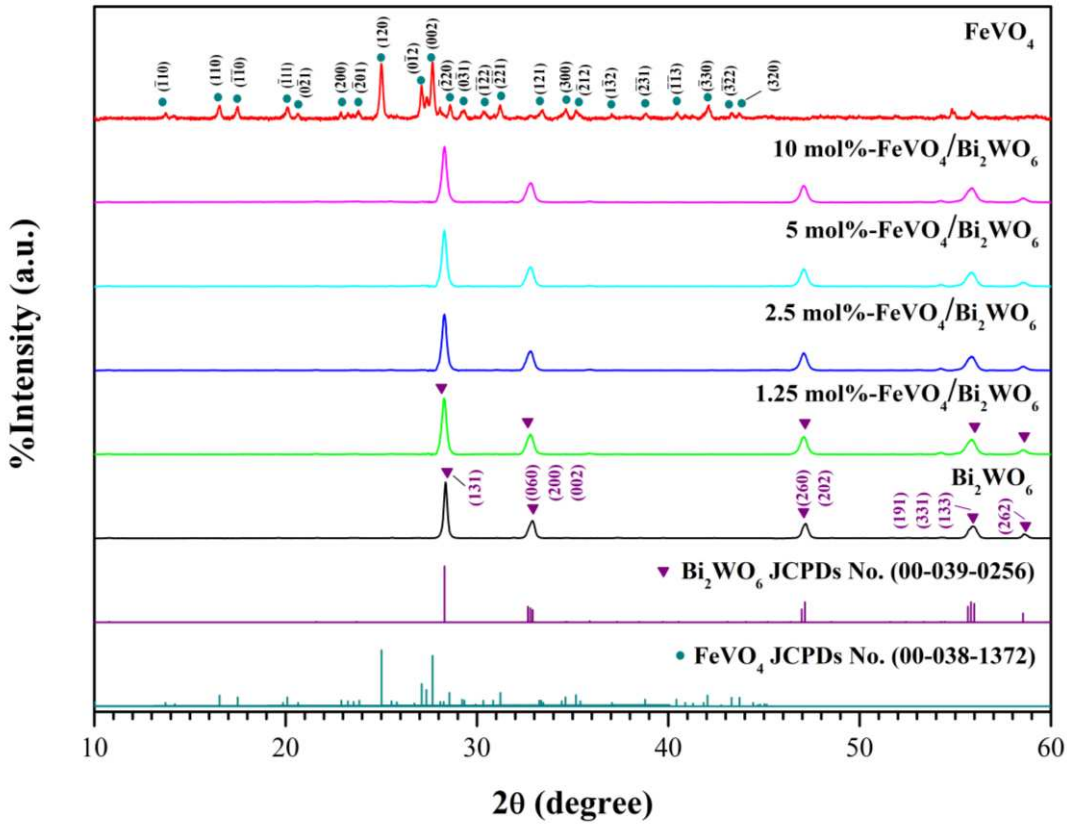

Fig. 1. XRD patterns of the Bi_2WO_6 and $FeVO_4$ powders and the $FeVO_4/Bi_2WO_6$ nanocomposites at varying contents of $FeVO_4$.

Fig. 2 shows the FESEM images of the Bi_2WO_6, $FeVO_4$, and 2.5 mol%-$FeVO_4/Bi_2WO_6$ powders. The Bi_2WO_6 (**Fig. 2**(a)) and $FeVO_4$ (**Fig. 2**(b)) powders are composed of spherical nanoparticles with diameters in 60–80 and 120–150 nm ranges, respectively, confirming the formation of nanosized particles and narrow size distributions via a microwave-assisted calcination process. Additionally, Bi_2WO_6 and $FeVO_4$ nanoparticles exhibit an aggregate behavior, driven by the minimization of their high surface energy. The FESEM image of 2.5 mol%-$FeVO_4/Bi_2WO_6$ (**Fig. 2**(c)) shows the indistinguishable shapes of the Bi_2WO_6 and $FeVO_4$ nanoparticles. TEM images (**Fig. 2**(e and f)) reveal the Bi_2WO_6 nanoparticles with a smaller size and $FeVO_4$ nanoparticles with a larger size attached to each other. **Fig. 2**(g and h) show high-magnification TEM images of a selected square area of the 2.5 mol%-

$FeVO_4/Bi_2WO_6$ nanocomposite. Two sets of lattice fringes with *d*-spacing values of **0.193 and 0.213 nm are observed corresponding to the (202) and ($\bar{3}$30) planes of the orthorhombic Bi_2WO_6 and tetragonal $FeVO_4$ crystalline structures, respectively,** confirming the attachment of Bi_2WO_6 and $FeVO_4$ nanoparticles to form $FeVO_4/Bi_2WO_6$ nanocomposite. The EDX spectrum of the 2.5 mol%-$FeVO_4/Bi_2WO_6$ nanocomposite (**Fig. 2**(d)) shows the characteristic peaks of Bi, W, Fe, V, and O, indicating the coexistence of $FeVO_4$ and Bi_2WO_6 in the nanocomposite. Additionally, scanning TEM-EDX elemental mapping (**Fig. 3**) reveals a homogeneous distribution of the elements throughout the nanocomposite. Therefore, the results confirm the close interfacial contact between the $FeVO_4$ and Bi_2WO_6 nanoparticles in the $FeVO_4/Bi_2WO_6$ heterojunction, which is important for facilitating the transfer of photogenerated charge carriers across the contact interface.

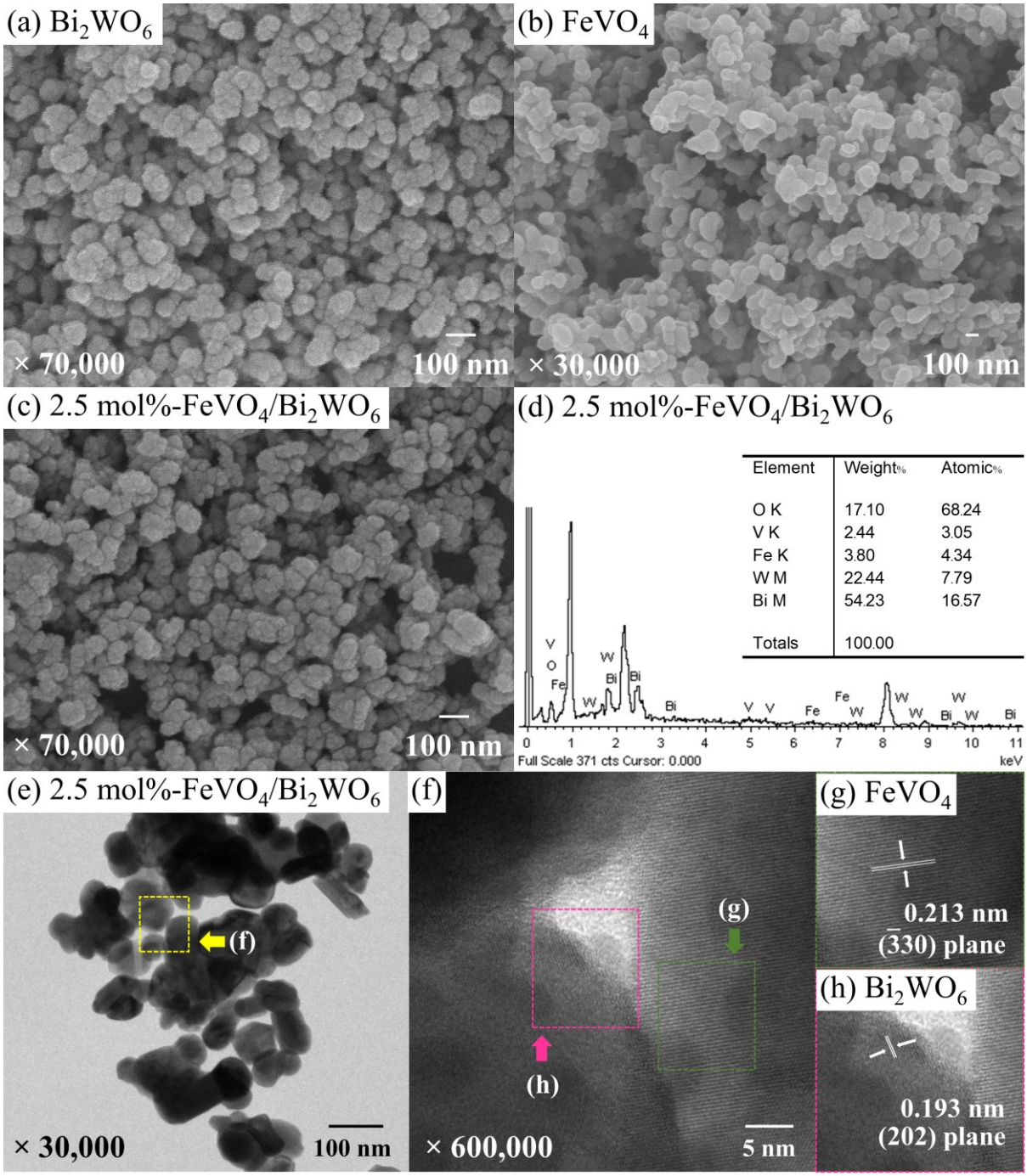

Fig. 2. FESEM images of (a) Bi_2WO_6, (b) $FeVO_4$, and (c) the 2.5 mol%-$FeVO_4/Bi_2WO_6$ nanocomposite. (d) EDX spectrum and (e and f) TEM images of the 2.5 mol%-$FeVO_4/Bi_2WO_6$ nanocomposite. (g and h) High-magnification TEM images of the selected square area shown in (f).

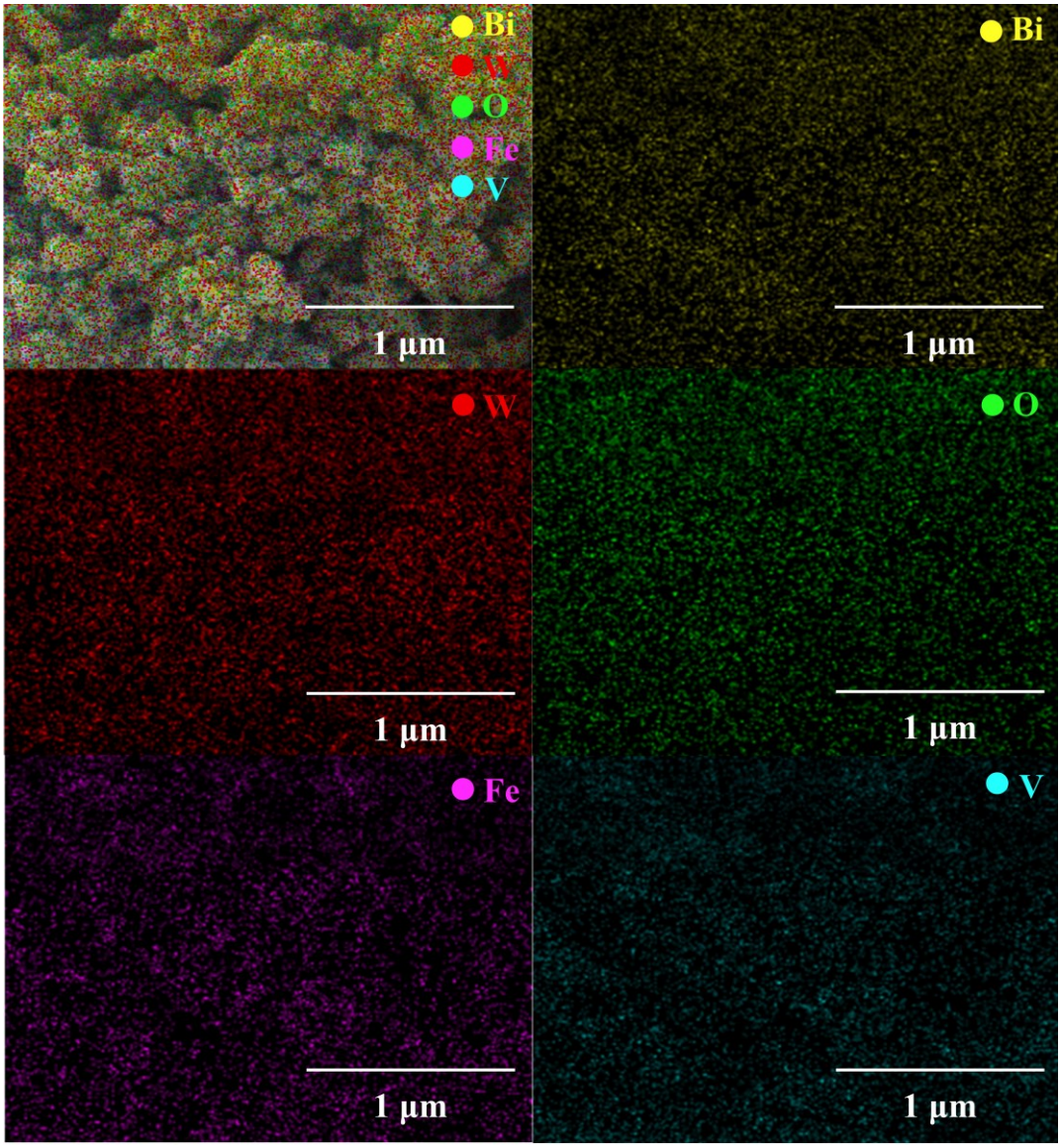

Fig. 3. Scanning TEM and the corresponding elemental mapping images of the 2.5 mol%-$FeVO_4/Bi_2WO_6$ nanocomposite.

XPS analysis was used to confirm the elemental composition, oxidation states of the synthesized samples, and chemical interaction of $FeVO_4$ and Bi_2WO_6 in the $FeVO_4/Bi_2WO_6$ heterostructure. The XPS survey spectrum of Bi_2WO_6 (Fig. 4(a)) shows the presence of Bi, W, and O elements, whereas the spectrum of $FeVO_4$ shows Fe, V, and O elements. For the 2.5 mol%-$FeVO_4/Bi_2WO_6$ nanocomposite, the signals for Bi, W, O, Fe, and V elements are observed. The C 1*s* peak at 284.7 eV is attributed to the

adventitious carbon species. The high-resolution XPS spectrum of Bi 4*f* (Fig. 4(b)) in Bi_2WO_6 shows two strong peaks at 158.1 and 163.4 eV corresponding to Bi $4f_{7/2}$ and Bi $4f_{5/2}$ of Bi^{3+} ion, respectively [38]. For 2.5%mol-$FeVO_4/Bi_2WO_6$, the Bi $4f_{7/2}$ and Bi $4f_{5/2}$ signals shift to 158.9 and 164.2 eV, respectively. As shown in Fig. 4(c), the two peaks of Bi_2WO_2 at 34.4 and 36.6 eV are assigned to W $4f_{7/2}$ and W $4f_{5/2}$ of W^{6+} ion, respectively [39], whereas the W $4f_{7/2}$ and W $4f_{5/2}$ peaks of 2.5 mol%-$FeVO_4/Bi_2WO_6$ shift to 35.1 and 37.3 eV, respectively. Fig. 4(d) shows the O 1*s* spectra of Bi_2WO_6, $FeVO_4$, and 2.5 mol%-$FeVO_4/Bi_2WO_6$. For Bi_2WO_6, three binding energy peaks are located at 529.1, 530.2, and 531.7 eV, which represent the coordination of oxygen in Bi–O, W–O, and the chemically absorbed oxygen (O-H) on its surface, respectively [38–41]. For $FeVO_4$, the O 1*s* peaks located at 530.5 and 532.6 eV are attributed to the chemical bonds of V–O and Fe–O, respectively [33–35]. For 2.5 mol%-$FeVO_4/Bi_2WO_6$, three sub-peaks located at 529.9, 531.1, and 532.5 eV are observed ascribed to the Bi–O and W–O bonds in the Bi_2WO_6 and O-H bonds in the surface-adsorbed oxygen, respectively. In Fig. 4(e), Fe $2p_{3/2}$ and Fe $2p_{1/2}$ peaks of Fe^{3+} ion for 2.5 mol%-$FeVO_4/Bi_2WO_6$ are observed at 710.5 and 524.0 eV, respectively, which are lower in energy compared with those of $FeVO_4$ (711.3 and 724.9 eV, respectively) [33–35]. The XPS spectrum of V 2*p* in 2.5 mol%-$FeVO_4/Bi_2WO_6$ (Fig. 4(f)) exhibits V $2p_{3/2}$ (516.6 eV) and V $2p_{1/2}$ (524.0 eV) of V^{5+} ion at lower energies compared with those in the $FeVO_4$ (V $2p_{3/2}$ (517.5 eV) and V $2p_{1/2}$ (525.1 eV)) [33–35]. The shifts in the binding energy of Bi 4*f*, W 4*f*, O 1*s*, Fe 2*p*, and V 2*p* for the $FeVO_4/Bi_2WO_6$ nanocomposite clearly confirm the existence of the $FeVO_4$ in the $FeVO_4/Bi_2WO_6$ nanocomposite and the interfacial chemical interaction between $FeVO_4$ and Bi_2WO_6 rather than a physical contact between each single-component material.

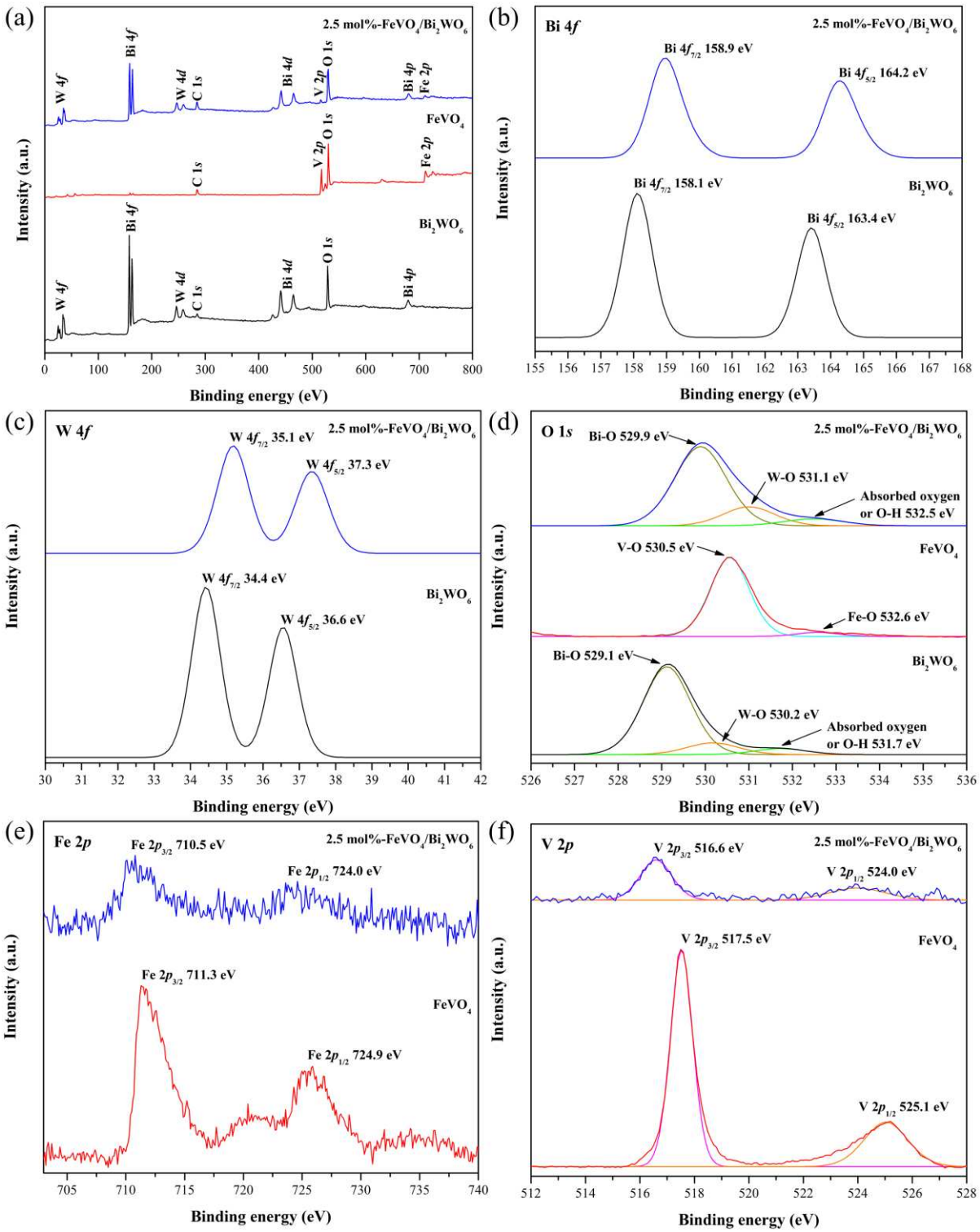

Fig. 4. (a) Survey XPS spectra of Bi_2WO_6, $FeVO_4$, and 2.5 mol%-$FeVO_4$/Bi_2WO_6. XPS spectra of (b) Bi 4*f*, (c) W 4*f*, (d) O 1*s*, (e) Fe 2*p*, and (f) V 2*p*.

3.2. Optical properties

The UV–vis DRS of Bi_2WO_6 and $FeVO_4$ (**Fig. 5**(a)) exhibit absorption edges at 445 and 577 nm, respectively. The absorption edge of the 2.5 mol%-$FeVO_4$/Bi_2WO_6 nanocomposite appears between those of the Bi_2WO_6 and $FeVO_4$ powders, corresponding to the color change of the Bi_2WO_6 after the addition of $FeVO_4$. **The red-shift of the absorption onset of the 2.5 mol%-$FeVO_4$/Bi_2WO_6 nanocomposite, compared with that of Bi_2WO_6, indicating that Bi_2WO_6 is coupled with $FeVO_4$. Additionally, the absorption intensity of the UV-vis DRS for the 2.5 mol%-$FeVO_4$/Bi_2WO_6 nanocomposite is considerably stronger than that for Bi_2WO_6. These results suggest that, compared to the Bi_2WO_6, coupling of Bi_2WO_6 with $FeVO_4$ can enhance the absorption ability in the visible light region, producing more photogenerated charge carriers for photocatalytic reactions.** To determine the energy bandgap (E_g) of the samples, the Tauc equation, $\alpha h\nu = A(h\nu - E_g)^{n/2}$, where α, h, ν, E_g, and A represent the absorption coefficient, Planck's constant, light frequency, energy bandgap, and proportional constant, respectively, was used. The n value is 1 and 4 for the direct and indirect bandgap materials, respectively, and for both Bi_2WO_6 and $FeVO_4$, n = 4 [16,34]. Using the $(\alpha h\nu)^{1/2}$ versus hν plots (**Fig. 5**(b)), the E_g values for Bi_2WO_6 and $FeVO_4$ are calculated as 2.78 and 2.06 eV, respectively.

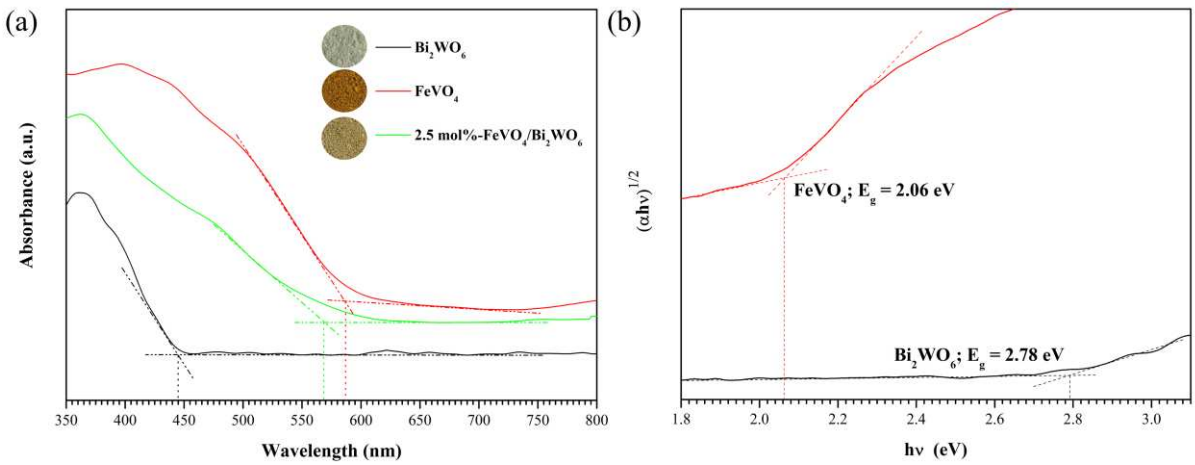

Fig. 5. (a) UV–vis DRS of Bi_2WO_6, $FeVO_4$, and 2.5 mol%-$FeVO_4/Bi_2WO_6$. (b) Tauc plots of Bi_2WO_6 and $FeVO_4$.

3.3. Electrochemical properties

The EIS Nyquist plots of the Bi_2WO_6, $FeVO_4$, and $FeVO_4/Bi_2WO_6$ film electrodes were recorded to evaluate the charge-transfer efficiency, and the results are shown in **Fig. 6**(a). The arc radius in an EIS Nyquist plot represents the charge transfer resistance across the electrode/electrolyte interface [42,43]. **The arc radius of all $FeVO_4/Bi_2WO_6$ electrodes is smaller than that of Bi_2WO_6 and $FeVO_4$ electrodes, implying that the charge transfer from the $FeVO_4/Bi_2WO_6$ electrodes to the electrolyte solution is improved. Among the $FeVO_4/Bi_2WO_6$ electrodes, the 2.5 mol%-$FeVO_4/Bi_2WO_6$ electrode exhibits the lowest arc radius, reflecting the lowest charge-transfer resistance of the electrode. This finding implies that the electrode has the highest level of effective charge-transfer efficiency at the electrode/electrolyte interface, and therefore, a large number of charge carriers take part in the photocatalytic reactions, which is essential for enhancing photocatalytic activity.** Additionally, the lifetime of the photogenerated electron (τ) in the Bi_2WO_6, $FeVO_4$, and 2.5 mol%-$FeVO_4/Bi_2WO_6$ photocatalysts could be determined from the Bode-phase plots using the equation $\tau = 1/(2\pi f)$, where f represents the inverse minimum frequency [43,44]. **From Fig. 6(b),** the inverse minimum frequencies of Bi_2WO_6, $FeVO_4$, and 2.5 mol%-$FeVO_4/Bi_2WO_6$ **are found to be** 12,589, 15,789, and 10,000 Hz, respectively, corresponding to the electron lifetimes of 12.6, 10.1, and 15.9 μs, respectively. The increase in the lifetime of the photogenerated electrons in 2.5 mol%-$FeVO_4/Bi_2WO_6$ confirms the more effective separation of photogenerated e^-/h^+ pairs and faster interfacial charge migration [15,45].

The intensity of the PL spectrum is directly proportional to the recombination of photogenerated e^-/h^+ pairs [46,47]. As shown in Fig. 6(c), the highest PL emission

intensity of Bi_2WO_6 implies that the recombination of charge carriers in Bi_2WO_6 is the highest among the materials investigated. The PL emission intensity of 2.5 mol%-$FeVO_4/Bi_2WO_6$ is lower than that of Bi_2WO_6, implying that the recombination rate for the photogenerated e^-/h^+ pairs decreases after coupling $FeVO_4$ with Bi_2WO_6 [14]. Moreover, the PL emission intensity of the $FeVO_4/Bi_2WO_6$ physical mixture, designated as P2.5 mol%-$FeVO_4/Bi_2WO_6$, is lower than that of Bi_2WO_6 and higher than that of 2.5%mol-$FeVO_4/Bi_2WO_6$ suggesting that the decrease in PL emission intensity of 2.5%mol-$FeVO_4/Bi_2WO_6$ originates via the suppression of recombination process of the photogenerated e^-/h^+ pairs in the nanocomposite material, and not due to the lowest PL emission intensity of $FeVO_4$.

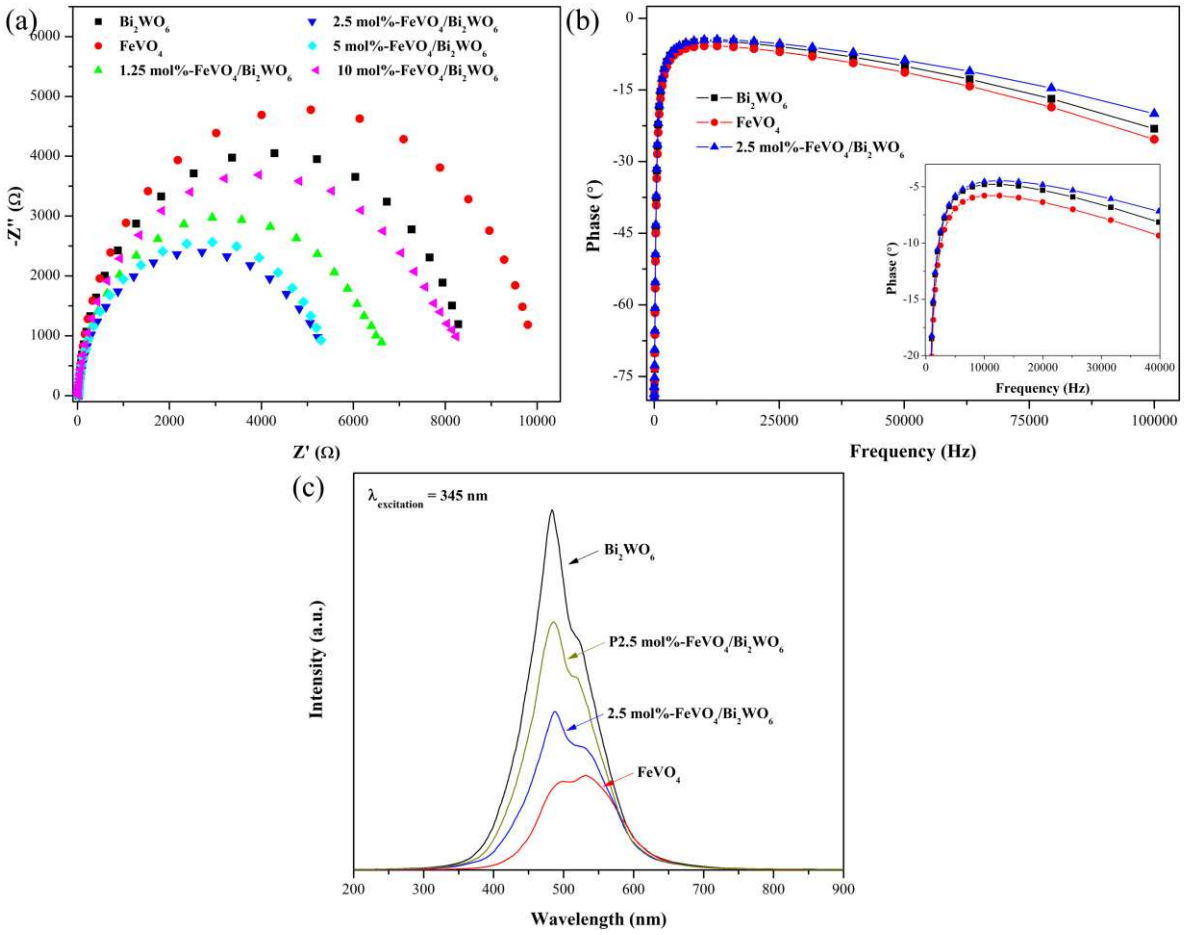

Fig. 6. (a) EIS Nyquist plots, (b) Bode-phase plots, and (c) PL spectra of the samples.

3.4. Photocatalytic activity

3.4.1. Photocatalytic degradation of organic pollutants

The photocatalytic activities of Bi_2WO_6, $FeVO_4$, and $FeVO_4/Bi_2WO_6$ for the photodegradation of BPA under visible-light irradiation are given in **Fig. 7**(a and b). **To eliminate the influence of physical adsorption, the photocatalytic system was kept in the dark for 30 min before light irradiation. The adsorption capacities of BPA by Bi_2WO_6, $FeVO_4$, and $FeVO_4/Bi_2WO_6$ are 15.9, 13.1, and 13.0%, respectively. After 330 min of light irradiation, 24.1 and 9.8% of BPA are photocatalytically degraded by Bi_2WO_6 and $FeVO_4$ with apparent rate constants (*k*) of 0.9×10^{-3} and 0.3×10^{-3} min^{-1}, respectively.** Compared to the individual Bi_2WO_6 and $FeVO_4$ photocatalysts, all $FeVO_4/Bi_2WO_6$ photocatalysts exhibit a higher %DE and *k* value. Among them, 2.5 mol%-$FeVO_4/Bi_2WO_6$ exhibits the best performance with a %DE of 65.1% and a *k* value of 3.0×10^{-3} min^{-1}, which is 3.3 and 10.0 times faster than those of Bi_2WO_6 and $FeVO_4$, respectively.

Photodegradation of MB was evaluated under identical photocatalytic conditions and the results are given in **Fig. 7**(c and d). **In the dark, 30.1, 36.3, and 35.4% of MB are adsorbed by Bi_2WO_6, $FeVO_4$, and $FeVO_4/Bi_2WO_6$, respectively.** After 330 min of light irradiation, 39.6 and 22.2% of MB are photocatalytically degraded by Bi_2WO_6 and $FeVO_4$ with the *k* values of 1.4×10^{-3} and 0.6×10^{-3} min^{-1}, respectively. Similar to BPA photodegradation, all the $FeVO_4/Bi_2WO_6$ photocatalysts provide higher %DE and *k* value than those of Bi_2WO_6 and $FeVO_4$. The 2.5 mol%-$FeVO_4/Bi_2WO_6$ photocatalyst exhibits the highest %DE (74.4%) and *k* value (3.7×10^{-3} min^{-1}) which is 2.6 and 6.1 times faster than that of Bi_2WO_6 (1.4×10^{-3} min^{-1}) and $FeVO_4$ (0.6×10^{-3} min^{-1}), respectively. In the absence of any photocatalyst, no significant change in the BPA and MB concentration is observed when their solutions are exposed to visible light, demonstrating that BPA and MB molecules are degraded via photocatalytic reactions. **Total organic carbon (TOC) analysis was performed to**

investigate the mineralization of BPA and MB using the synthesized photocatalysts, and the results are presented in Fig. 8(a). After light irradiation for 330 min, the TOC removals for the photodegradation of BPA and MB by 2.5 mol%-$FeVO_4/Bi_2WO_6$ are 53.8 and 62.1%, respectively. For Bi_2WO_6, the photodegradation efficiencies of BPA and MB are 16.9 and 24.2%, respectively. These findings confirm that, compared with that of pure Bi_2WO_6, the 2.5 mol%-$FeVO_4/Bi_2WO_6$ photocatalyst exhibits stronger mineralization ability, and a majority of the BPA and MB molecules are mineralized during the photodegradation process.

Based on the BPA and MB photodegradation tests, it can be concluded that the optimum content of $FeVO_4$ for the maximum photocatalytic activity of the $FeVO_4/Bi_2WO_6$ nanocomposite is 2.5 mol%. As the $FeVO_4$ content was increased (5 and 10 %mol), the photocatalytic activity of the nanocomposites decreased due to an excessive number of low-performing $FeVO_4$ nanoparticles shielding the surface-active sites of the photocatalyst. The degradation of BPA and MB diminished due to the lower $FeVO_4$ content (1.25 mol%) attached to the Bi_2WO_6 surface. Inappropriate amounts of the individual components in the $FeVO_4/Bi_2WO_6$ nanocomposites could not efficiently overcome the rapid e^-/h^+ pair recombination, which consequently decreased the photocatalytic efficiency. Furthermore, the photocatalytic activity of a physical mixture of 2.5 mol%-$FeVO_4$ and Bi_2WO_6 (P2.5 mol%-$FeVO_4/Bi_2WO_6$) did not enhance the degradation of BPA or MB compared to that of the single Bi_2WO_4 photocatalyst. Additionally, the activity of this mixture was significantly lower than that of the 2.5 mol%-$FeVO_4/Bi_2WO_6$ photocatalyst, indicating that the $FeVO_4/Bi_2WO_6$ heterojunction was formed via chemical interactions rather than simple physical interactions.

The N_2 adsorption–desorption isotherm and pore size distribution of 2.5 mol%-$FeVO_4/Bi_2WO_6$ in comparison with Bi_2WO_6 and $FeVO_4$ are presented in Fig. S4, and the corresponding data are given in Table S1. The isotherms of the photocatalyst samples

correspond to type IV behavior and the pore size distribution curves reveal that the photocatalyst samples have mesopores with average pore diameters in 31–35 Å range. It should be noted that these photocatalysts present a non-porous structure with some porosity owing to the aggregation of nanoparticles as revealed in Fig. 2. The BET surface area and total pore volume of Bi_2WO_6 are 7.361 $m^2 g^{-1}$, and 0.04115 $cm^3 g^{-1}$, respectively. For $FeVO_4$, the corresponding values are 15.537 $m^2 g^{-1}$, and 0.04491 $cm^3 g^{-1}$, respectively. After incorporating $FeVO_4$, the surface area of 2.5%mol-$FeVO_4/Bi_2WO_6$ appears to be decreased due to the close contact of the Bi_2WO_6 and $FeVO_4$ nanoparticles (9.332 $m^2 g^{-1}$). However, the results from the photocatalytic activity experiments reveal that 2.5 mol%-$FeVO_4/Bi_2WO_6$ still exhibits the highest photocatalytic activity, although the adsorption abilities of these photocatalysts toward either BPA or MB molecules are insubstantially different (Fig. 7). Therefore, in this study, the surface area could not be a key factor for enhancing the photocatalytic activity. Notably, a larger total pore volume of 2.5 mol%-$FeVO_4/Bi_2WO_6$ (0.06235 $cm^3 g^{-1}$) could be caused by the aggregated and interlinked nanocrystals, which benefit to the intraparticle charge transfer [48]. The improved optical and electrochemical properties upon coupling Bi_2WO_6 with $FeVO_4$ are among the key factors enhancing photocatalytic activity of the heterojunction as discussed above.

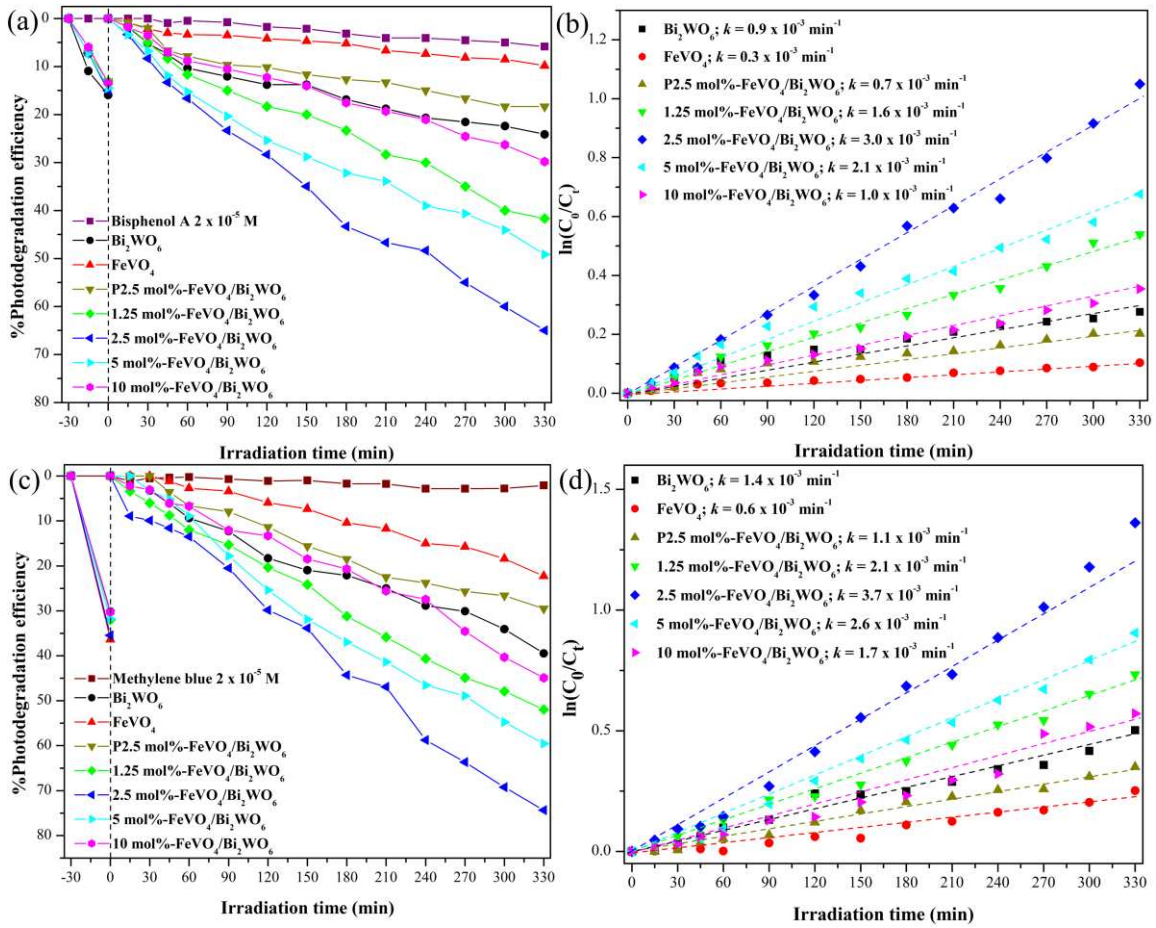

Fig. 7. Photodegradation efficiency and the corresponding kinetic plots of photodegradation for (a and b) BPA and (c and d) MB, respectively, by the Bi_2WO_6, $FeVO_4$, and $FeVO_4/Bi_2WO_6$ photocatalysts.

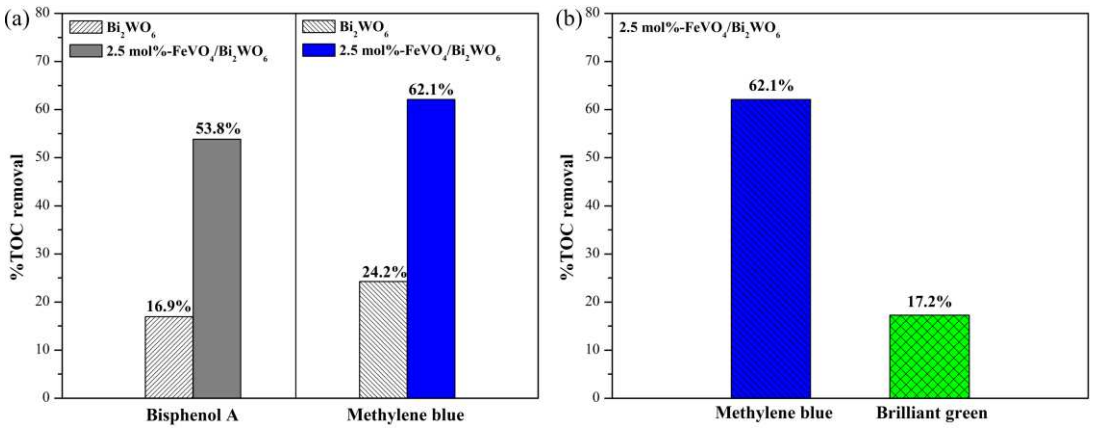

Fig. 8. (a) %TOC removal using 2.5 mol%-$FeVO_4/Bi_2WO_6$ for (a) BPA and MB in comparison with that of Bi_2WO_6, and (c) MB and BG under 330 min of visible-light irradiation.

Further, the effects of photocatalyst dosage, organic dye concentration, and type of organic dye on the photodegradation rate were investigated. **Fig. S5**(a) reveals the highest photodegradation rate ($k = 3.7 \times 10^{-3}$ min^{-1}) at the MB concentration of 2×10^{-5} M and 100 mg of photocatalyst loading; the k values are 1.8 and 3.7 times higher than that at 50 ($k = 2.0 \times 10^{-3}$ min^{-1}) and 150 mg ($k = 1.0 \times 10^{-3}$ min^{-1}) of photocatalyst loading. At a lower photocatalyst loading of 50 mg, a lower photodegradation rate is observed because the available active sites on the photocatalyst surface are not sufficient for the adsorption of MB molecules for degradation [49]. At a higher photocatalyst loading of 150 mg, the suspension become turbid owing to the agglomeration of the photocatalytic particles that inhibits visible-light penetration [50]. **By fixing the amount of the 2.5 mol%-$FeVO_4/Bi_2WO_6$ photocatalyst at 100 mg, the initial MB concentration was varied to investigate the photoefficacy of the photocatalyst. Fig. S5(b) reveals that as the initial MB concentration gradually increases from 1×10^{-5} to 2×10^{-5}, and 4×10^{-5} mol L^{-1}, the k values decrease from 4.3×10^{-3} to 3.7×10^{-3}, and 1.5×10^{-3} min^{-1}, respectively owing to the limited availability of the photocatalytic active sites for the photocatalytic reaction, and the opacity of the MB solution which hinders the penetration of light into the solution [13].**

The photodegradation efficiency of the 2.5 mol%-$FeVO_4/Bi_2WO_6$ photocatalyst for other organic dyes, including BG and MO, was further investigated, and the results are represented in **Fig. 9**(a and b). After 330 min of visible-light irradiation, 34.5 and 2.0% of BG and MO are degraded showing k values of 1.1×10^{-3} and 0.09×10^{-3} min^{-1}, which are 3.4 and 41.1 times lower than that for MB photodegradation (%DE = 74.4%, $k = 3.7 \times 10^{-3}$ min^{-1}), respectively. The difference in the photocatalytic efficiency could influence the adsorption capability of these dyes on the surface of the photocatalyst. To verify this assumption, the surface charge of the 2.5 mol%-$FeVO_4/Bi_2WO_6$ photocatalyst was determined by measuring

its pH_{PZC}. **Fig. S6**(a) shows that the pH_{PZC} of the photocatalyst is 4.47. At the measured pH of 6–7 approximately, the photocatalyst carries a negative charge. The negatively charged surface favors the efficient adsorption of cationic dye molecules (MB and BG) over the anionic dye molecules (MO) to access the active sites via electrostatic interaction and subsequent photodegradation, thereby promoting photodegradation efficiency [51]. The higher %DE of MB than that of BG is attributed to the higher adsorption ability of the MB molecules on the 2.5 mol%-$FeVO_4/Bi_2WO_6$ surface; 35.4% of MB and 20% of BG are absorbed (**Fig. S7**).

The changes in the UV–vis absorption spectra for the photodegradation of MB and BG solutions in the presence of the 2.5 mol%-$FeVO_4/Bi_2WO_6$ photocatalyst at different irradiation times are shown in **Fig. 9**(c and d), respectively. The intensities of the characteristic absorption peaks for MB and BG gradually decrease with increasing reaction time. No shift in the maximum absorption peak of MB is observed during 0–300 min of the reaction; however, the peak wavelength slightly shifts at 330 min, implying that the cleavage of the chromophore structure is predominant, and *N*-de-methylation occurs to a lesser extent [16,52,53]. In contrast, the maximum absorption peak of BG shifts slightly to shorter wavelengths after prolonged reaction times, suggesting the *N*-de-ethylation photodegradation of BG [51]. **In terms of the chemical structure; MB is a heterocyclic aromatic dye containing two aromatic rings and a central heterocyclic ring, and BG is a triphenylmethane dye with three phenyl groups attached to a central carbon atom (Fig. 10). The *N*,*N*-diethyl and *N*-ethyl groups of BG could be attacked by active oxygen species generated from the photocatalyst, yielding a series of *N*-de-ethylated intermediates in a stepwise manner [51]. In contrast, the N-S heterocycle group of MB could be attacked by hydroxyl radicals (•OH) and oxidized to open the aromatic ring [52,54]. Additionally, the MB molecule has less steric hindrance and adopts a more planar symmetrical molecular structure, which makes it more suitable for adsorption on the photocatalyst surface; thus, resulting in aromatic-ring-opening**

reactions during photocatalytic degradation, which can decompose easily [53]. The TOC removal for the photodegradation of MB by 2.5 mol%-$FeVO_4/Bi_2WO_6$ (Fig. 8(b)) is 62.1%, which is 3.6 times higher than that for the photodegradation of BG (TOC removal = 17.2%).

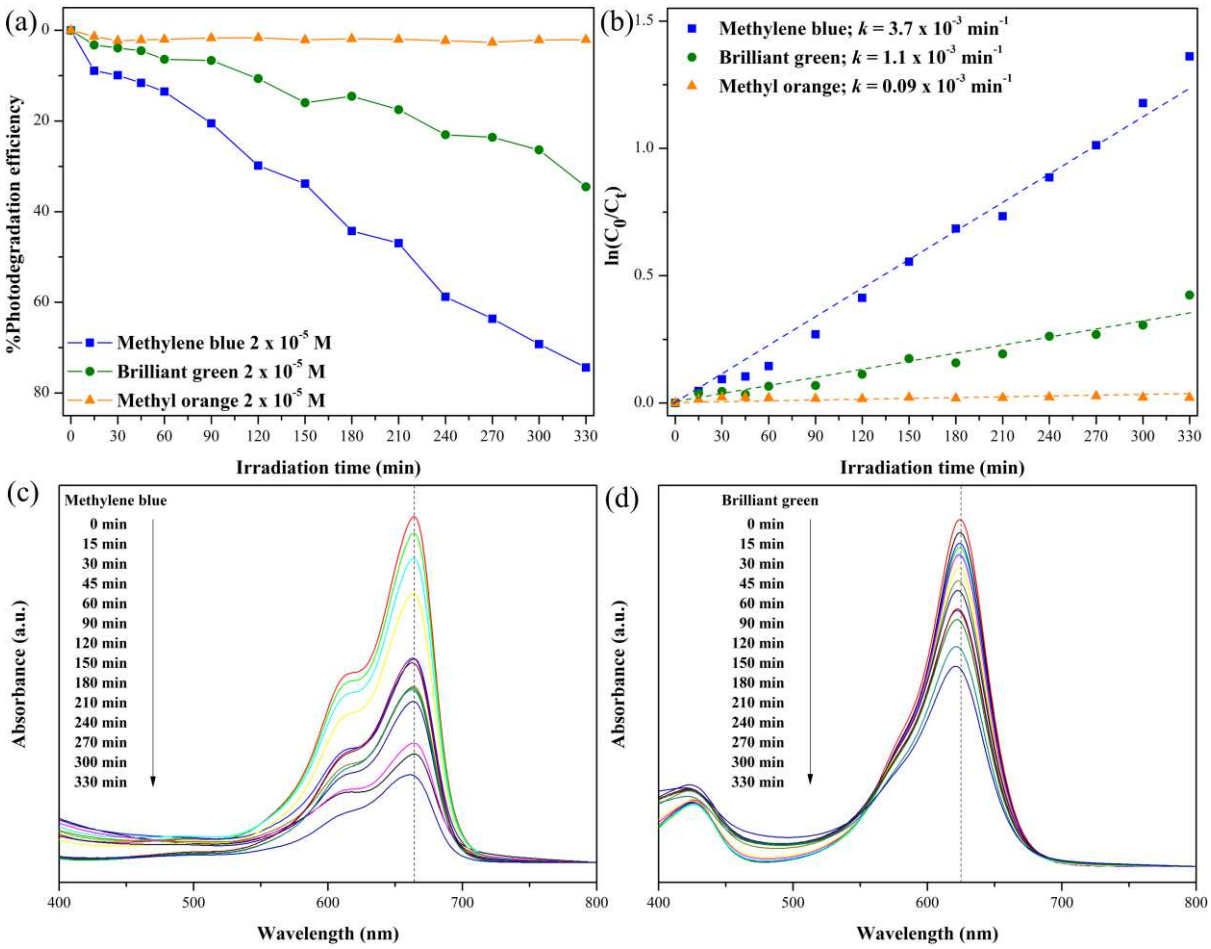

Fig. 9. (a and b) Effect of different organic dyes on the photocatalytic activity of the 2.5 mol%-$FeVO_4/Bi_2WO_6$ photocatalyst. **Changes in the UV–vis absorption spectra of (c) MB and (d) BG solutions in the presence of the 2.5 mol%-$FeVO_4/Bi_2WO_6$ photocatalyst at different irradiation times.**

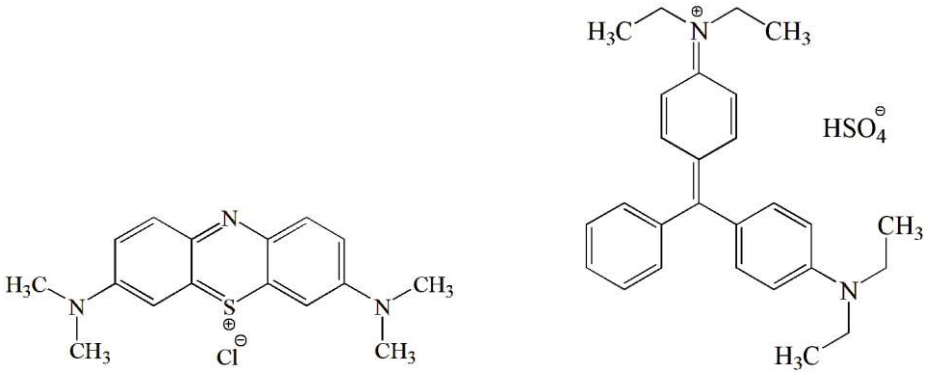

Methylene blue (MB) Brilliant green (BG)

Fig. 10. Chemical structures of MB and BG.

3.4.2. Recyclability and stability of 2.5 mol%-$FeVO_4/Bi_2WO_6$

To determine the recyclability of the 2.5 mol%-$FeVO_4/Bi_2WO_6$ photocatalyst, three recycling tests were performed for the photodegradation of BPA and MB, as given in **Fig. 11**(a, b). After three recycling runs, a slight decrease in the %DE is observed for the photodegradation of BPA (6.1%) and MB (8.7%). The greater decrease in the %DE of MB compared to that of BPA could be attributed to the massive adsorption of MB on the surface of the photocatalyst (**Fig. S8**), blocking the absorption of incident light and consequently decreasing the production of photogenerated charges. The FESEM images of the used photocatalysts after three recycling runs (**Fig. 11**(c–e)) show no obvious differences compared to those of the fresh photocatalyst. Additionally, no diffraction peaks corresponding to the impurity phase are detected in the XRD patterns of the photocatalysts (**Fig. 11**(f)), which confirms the high photostability and recyclability of the 2.5 mol%-$FeVO_4/Bi_2WO_6$ photocatalyst for the degradation of either colorless or organic dye pollutants.

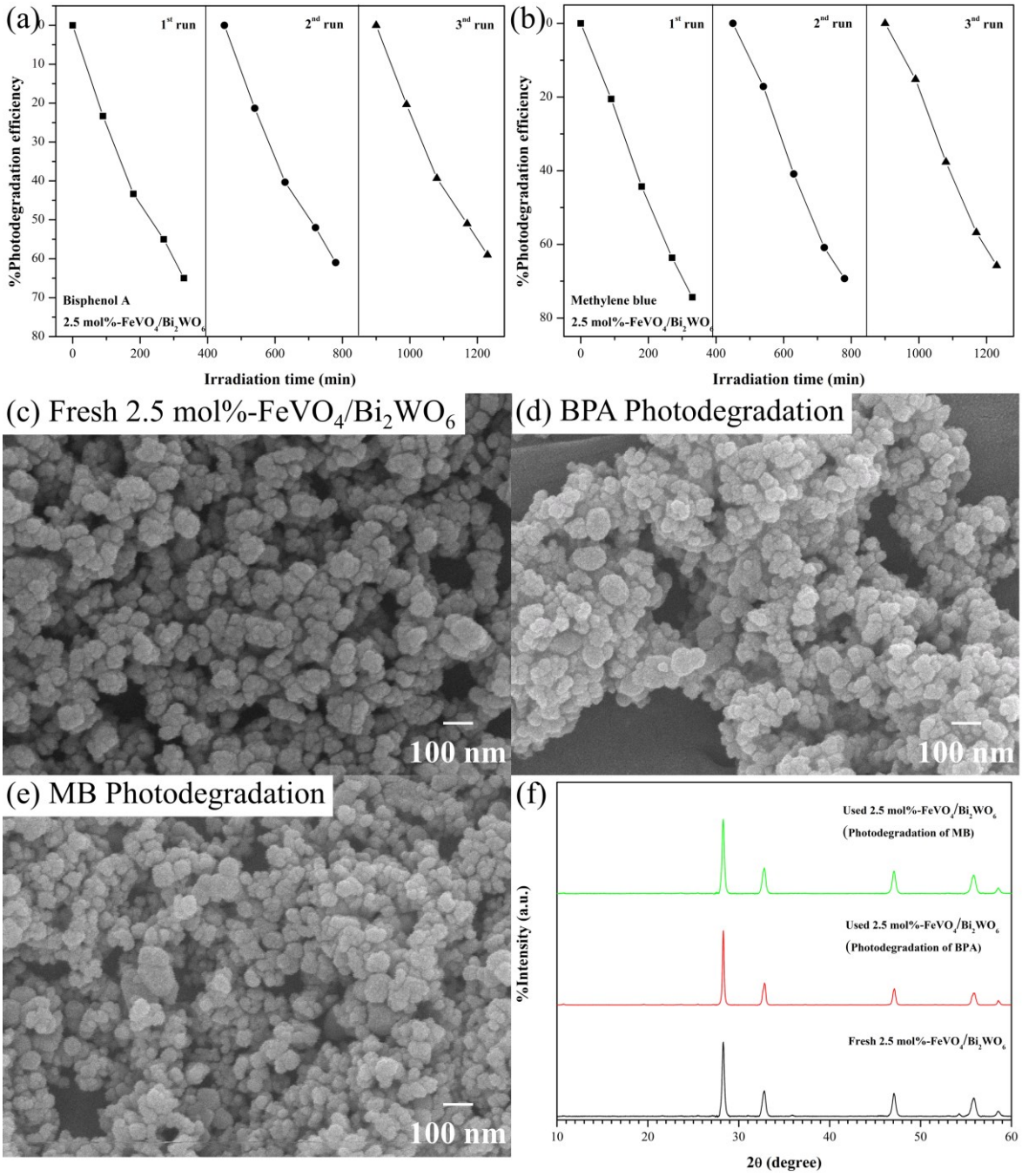

Fig. 11. Recyclability and stability of the 2.5 mol%-$FeVO_4/Bi_2WO_6$ photocatalyst after three cycles of the degradation of (a) BPA and (b) MB. (c–e) FESEM images and (f) XRD patterns of the used 2.5 mol%-$FeVO_4/Bi_2WO_6$ photocatalyst in comparison with that of the fresh photocatalyst.

3.5. Enhanced photocatalytic activity

3.5.1. Band positions of Bi_2WO_6 and $FeVO_4$

The flat-band potentials (E_{FB}) of Bi_2WO_6 and $FeVO_4$ were determined from the Mott–Schottky plots recorded at a frequency of 10 Hz. As shown in **Fig. 12**, the slopes of the linear Mott–Schottky plots of the Bi_2WO_6 and $FeVO_4$ electrodes are positive, indicating that Bi_2WO_6 and $FeVO_4$ are n-type semiconductors. By extrapolating the linear portion of the Mott–Schottky plots, the E_{FB} of the Bi_2WO_6 and $FeVO_4$ are –0.32 and –0.53 V (*vs.* NHE), respectively. The CB potential (E_{CB}) of an n-type semiconductor is more negative by –0.1 V (*vs.* NHE) compared to the E_{FB} value [55]. Therefore, the E_{CB} of Bi_2WO_6 and $FeVO_4$ are –0.42 and –0.63 V (*vs.* NHE), respectively. Subsequently, based on the theoretical equation $E_{VB} = E_{CB} + E_g$, the valence band potentials (E_{VB}) of Bi_2WO_6 and $FeVO_4$ are calculated as 2.36 and 1.43 V (*vs.* NHE), respectively.

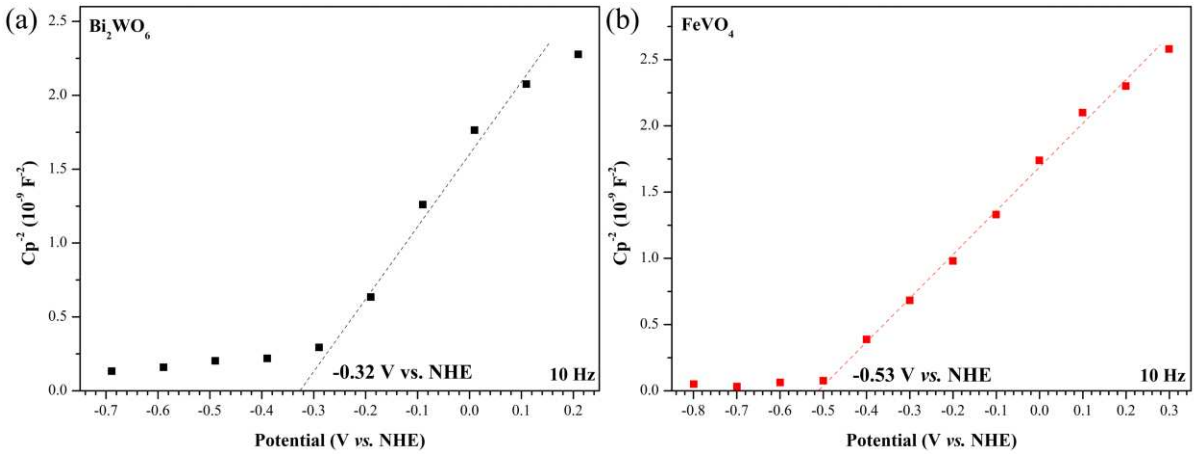

Fig. 12. Mott–Schottky plots of (a) Bi_2WO_6 and (b) $FeVO_4$.

3.5.2. Main reactive species

To identify the primary reactive species, different scavengers were introduced to trap the relevant reactive species over the 2.5 mol%-$FeVO_4$/Bi_2WO_6 photocatalyst, and the results are shown in **Fig. 13**. The addition of dimethyl sulfoxide (DMSO) or isopropanol (IPA), *p*-

benzoquinone (BQ), and $AgNO_3$ to a suspension of the photocatalyst and the targeted organic pollutant solution (BPA and MB) considerably decreases the photodegradation efficiency of BPA and MB. The result indicates that hydroxyl radicals (•OH), superoxide radicals ($•O_2^-$), and electrons (e^-) are the major reactive species involved in photocatalytic reactions. However, the addition of ammonium oxalate (AO) slightly decreases the %DE, indicating that hole (h^+) is a minor specie.

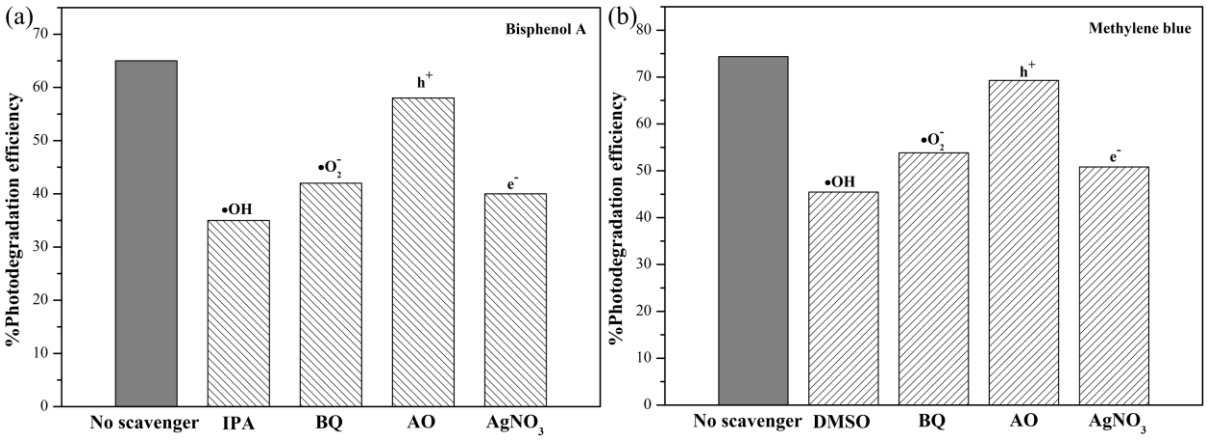

Fig. 13. Photodegradation efficiency of (a) BPA and (b) MB by the 2.5 mol%-$FeVO_4/Bi_2WO_6$ photocatalyst after the addition of different scavengers.

The nitroblue tetrazolium (NBT) transformation method was used to comprehend the production of $•O_2^-$ radicals during photocatalysis [16,56] as the $•O_2^-$ radicals directly react with NBT in a 1:4 molar ratio afford a formazan derivative [57]. The absorption spectra of the NBT supernatant solutions after 330 min of visible-light irradiation are shown in **Fig. 14**(a). The 2.5 mol%-$FeVO_4/Bi_2WO_6$ photocatalyst exhibits a lower intensity of absorption peak compared to that of the Bi_2WO_6 photocatalyst. The decrease in absorbance indicates a higher NBT conversion, which correlates with the increase in photogenerated $•O_2^-$ radicals. The NBT transformation percentage was calculated from the decrease in the absorption intensity of the NBT solution at λ_{max} = 265 nm. **Fig. 14**(b) presents that the 2.5 mol%-$FeVO_4/Bi_2WO_6$ photocatalyst shows a higher NBT transformation percentage (70.9%) than that of the Bi_2WO_6

photocatalyst (49.5%). The calculated yields of photogenerated $\bullet O_2^-$ radicals were 24.7 and 18.6 μmol L^{-1} for 2.5 mol%-$FeVO_4/Bi_2WO_6$ and Bi_2WO_6, respectively (**Fig. 14**(b)). These results imply that the 2.5 mol%-$FeVO_4/Bi_2WO_6$ heterojunction photocatalyst is more effective in generating $\bullet O_2^-$ radicals under visible-light irradiation than that using a single Bi_2WO_6 photocatalyst.

The generation of •OH radicals was confirmed via terephthalic acid photoluminescence (TA-PL) probing [56]. The •OH radicals produced during photocatalysis can react with TA to produce fluorescent 2-hydroxyterephathalic acid (TAOH), which emits fluorescence at 425 nm. The fluorescence intensity of the TAOH solution is directly proportional to the number of •OH radicals generated. As shown in **Fig. 14**(c), the peak intensity of TAOH gradually increases from 0 to 330 min of irradiation suggesting that •OH radicals generated in the photocatalytic reaction were produced through a process involving $\bullet O_2^-$ to H_2O_2 conversion via a multielectron oxygen reduction [56,58,59]. The result is consistent with those obtained from the scavenging of reactive species. The formation of H_2O_2 was verified using the *o*-tolidine spectrophotometric technique [60,61]. H_2O_2 reacts with *o*-tolidine yielding the protonated 2-electron oxidation product of *o*-tolidine, which shows the characteristic peak at approximately 446 nm. **Fig. 14**(d) shows that the absorbance of the 2-electron oxidized *o*-tolidine gradually increases upon visible-light irradiation, indicating that H_2O_2 is produced during the photocatalytic reaction.

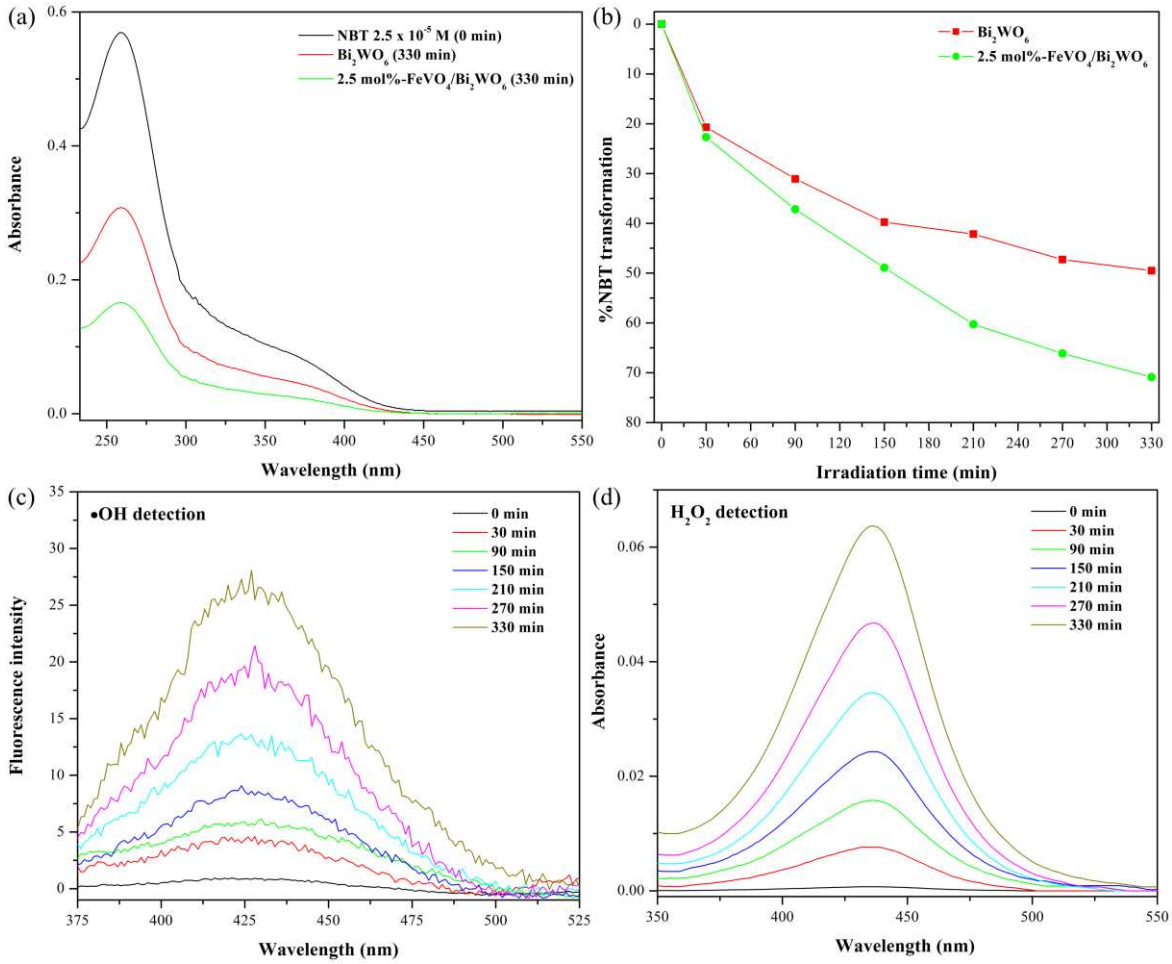

Fig. 14. (a) Absorption spectra of the NBT supernatant solutions catalyzed by the 2.5 mol%-$FeVO_4/Bi_2WO_6$ and Bi_2WO_6 after 330 min of visible-light irradiation. (b) %NBT transformation over the 2.5 mol%-$FeVO_4/Bi_2WO_6$ photocatalyst during 0–330 min of visible-light irradiation. (c) Fluorescence spectra of the TAOH solution were obtained at an excitation wavelength (λ_{ex}) of 315 nm. (d) UV–vis absorption spectra of the 2-electron oxidized *o*-tolidine over the 2.5 mol%-$FeVO_4/Bi_2WO_6$ photocatalyst.

3.5.3. Charge transfer pathway and mechanism

The staggered band alignment of the $FeVO_4/Bi_2WO_6$ heterojunction and the photogenerated charge transfer process are presented in **Fig. 15**. **These phenomena are reasoned out based on a comprehensive analysis of the Mott–Schottky plots, UV–vis DRS, and investigation of the main reactive species.** There are two possible charge-transfer

mechanisms for this heterojunction: conventional and direct Z-scheme charge-transfer mechanisms. In the conventional charge-transfer mechanism (**Fig. 15**(a)), both Bi_2WO_6 and $FeVO_4$ in the $FeVO_4/Bi_2WO_6$ heterojunction generate e^- and h^+ in their CB and VB, respectively, under visible-light irradiation. Subsequently, the photoexcited e^- migrates from the CB of $FeVO_4$ to the CB of Bi_2WO_6, and h^+ transfers from the VB of Bi_2WO_6 to the VB of $FeVO_4$ owing to the differences in the band potentials of these semiconductors. According to this charge-transfer pathway, the E_{CB} of Bi_2WO_6 (–0.42 V) is more negative than the reduction potential of $O_2/{\bullet}O_2^-$ (–0.046 V *vs.* NHE). Therefore, e^- accumulated at the CB of Bi_2WO_6 reduces O_2 to ${\bullet}O_2^-$. However, h^+ accumulated at the VB of $FeVO_4$ cannot oxidize OH^- to •OH owing to the less positive E_{VB} of $FeVO_4$ (+1.43 V) than the reduction potential of $\bullet OH/OH^-$ (+2.40 V *vs.* NHE), **which is inconsistent with the results obtained from the scavenging experiments and TA-PL probing technique.**

To further clarify the photocatalytic mechanism in the proposed reaction systems, the distribution of •OH and $\bullet O_2^-$ were investigated by ESR spin-trapping technique. Fig. 16(a and b) shows the EPR signals in methanol and aqueous dispersion with DMPO as the spin-trapping reagent for •OH and $\bullet O_2^-$ at 10 min of visible-light irradiation, respectively. In Fig. 16(a), both Bi_2WO_6 and 2.5 mol%-$FeVO_4/Bi_2WO_6$ exhibit the signals of DMPO-$\bullet O_2^-$, although slightly low, indicating that these photocatalysts create $\bullet O_2^-$ under visible-light irradiation. The peak intensity of DMPO-$\bullet O_2^-$ generated by 2.5 mol%-$FeVO_4/Bi_2WO_6$ is stronger than that generated by Bi_2WO_6, implying better $\bullet O_2^-$ generation ability. This result agrees with the NBT measurements. In Fig. 16(b), the DMPO-•OH signals are also observed for 2.5%mol-$FeVO_4/Bi_2WO_6$, whereas no obvious DMPO-•OH signals are detected for Bi_2WO_6, suggesting that h^+ in the VB of Bi_2WO_6 cannot generate •OH. Noticeably, 2.5 mol%-$FeVO_4/Bi_2WO_6$ exhibits drastically stronger signals of DMPO-•OH than DMPO-$\bullet O_2^-$, evidencing that most $\bullet O_2^-$ is converted to •OH.

This finding is consistent with the results obtained from the investigation of the main reactive species, in which the photocatalytic reaction is primarily driven by •OH, e^-, and $•O_2^-$, respectively. Therefore, •OH could be generated by activating molecular oxygen as mentioned above [58,59]. This means that e^- should be accumulated at the CB of $FeVO_4$ rather than CB of Bi_2WO_6 to get more powerful ability to reduce O_2 to $•O_2^-$. Subsequently, $•O_2^-$ is further reduced by the e^- to produce H_2O_2, and then generates highly reactive •OH oxidizing agent. Therefore, the charge-transfer mechanism in the $FeVO_4/Bi_2WO_6$ heterojunction could occur through a direct Z-scheme charge-transfer mechanism, as shown in Fig. 15(b).

In the direct Z-scheme charge-transfer mechanism, when the $FeVO_4/Bi_2WO_6$ heterojunction photocatalyst is exposed to visible light, Bi_2WO_6 and $FeVO_4$ generate e^-/h^+ pairs. Simultaneously, e^- in the CB of Bi_2WO_6 (–0.42 V) transfers to the VB of $FeVO_4$ (+1.43 V) because of the more positive E_{VB} of $FeVO_4$ and combines with h^+ in the VB of $FeVO_4$. Consequently, the photogenerated e^- with strong reducing ability reserved in the CB of $FeVO_4$ can produce $•O_2^-$ via the reduction of O_2 because of its more negative CB potential (–0.63 V) than the reduction potential of $O_2/•O_2^-$ (–0.046 V *vs.* NHE). Additionally, some $•O_2^-$ radicals are reduced to H_2O_2 molecules owning to the more negative value of the reduction potential of $O_2/•O_2^-$ than that of O_2/H_2O_2 (+0.68 V *vs.* NHE). Eventually, H_2O_2 molecules dissociate into highly reactive •OH radicals, which can oxidize BPA and MB molecules together with $•O_2^-$ radicals [59], **resulting in superior photocatalytic activity of the $FeVO_4/Bi_2WO_6$ heterojunction photocatalyst**. Simultaneously, residual h^+ in the VB of Bi_2WO_6 can directly react with BPA and MB molecules. These results corroborate well with those obtained from the scavenging experiments, NBT method, TA-PL technique, oxidation of *o*-tolidine by H_2O_2, **and ESR measurements**.

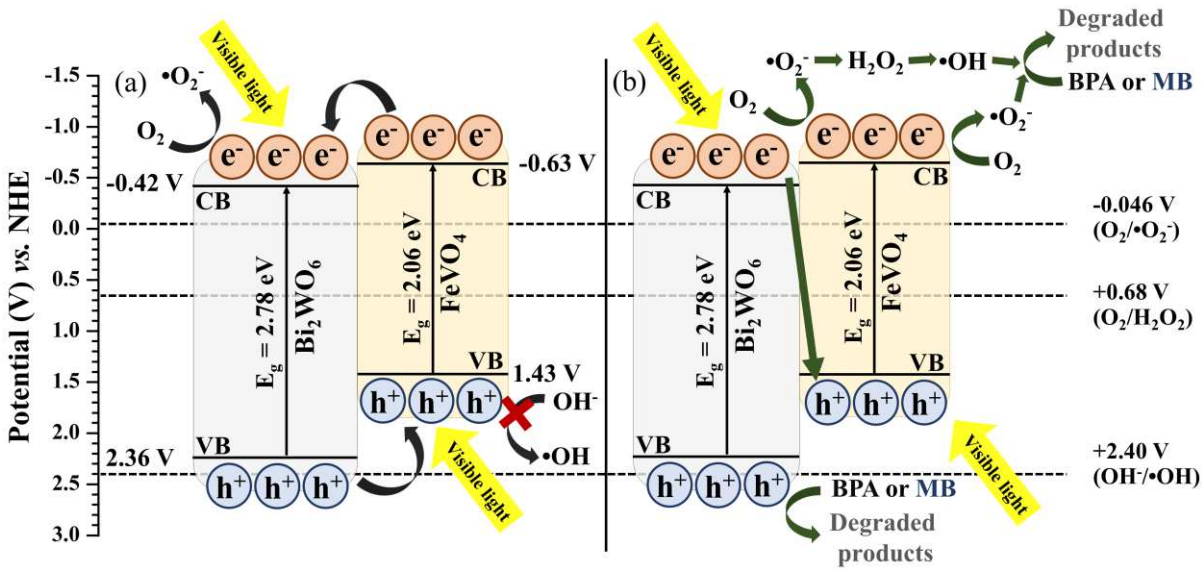

Fig. 15. Proposed band alignments and photogenerated charges transfer in $FeVO_4/Bi_2WO_6$ via (a) conventional and (b) direct Z-scheme charge-transfer processes.

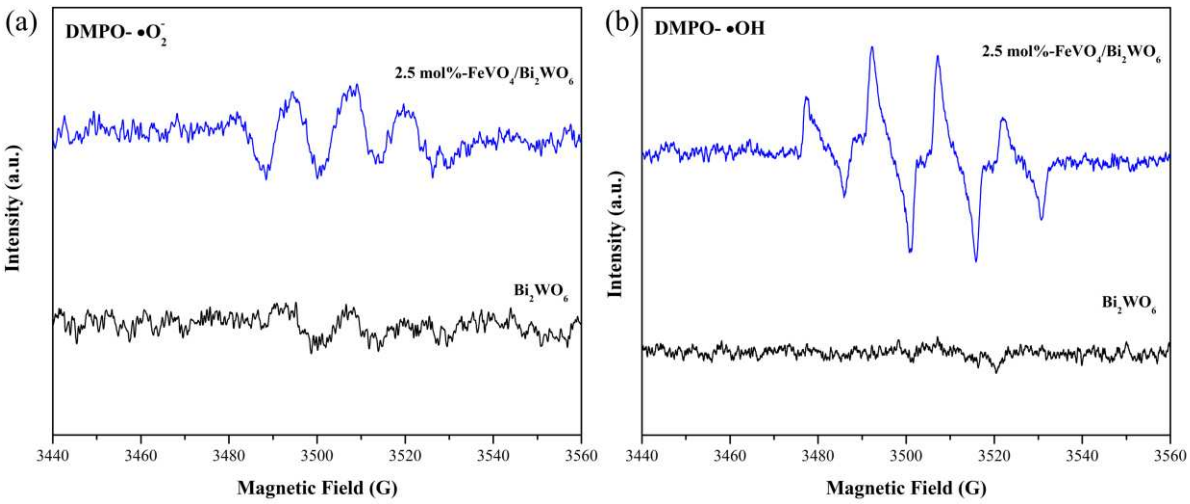

Fig. 16. ESR signals of (a) DMPO-•O_2^- and (b) DMPO-•OH adducts on Bi_2WO_6, and 2.5 mol%-$FeVO_4/Bi_2WO_6$ under 10 min of visible-light irradiation.

Moreover, PbO_2 and Ag photodeposition experiments were conducted to establish the direct Z-scheme charge-transfer process in the $FeVO_4/Bi_2WO_6$ heterojunction. Under light irradiation, the Pb^{2+} ions in $Pb(NO_3)_2$ can be oxidized to PbO_2 by accepting holes, and Ag^+ ions in $AgNO_3$ can be reduced to Ag by accepting electrons [34]. The HRTEM images of the 2.5

mol%-$FeVO_4/Bi_2WO_6$ photocatalyst after photodeposition using PbO_2 and Ag are shown in **Fig. 17**. The HRTEM images indicated that PbO_2 nanoparticles with a lattice spacing of 0.278 and 0.269 nm, corresponding to the (101) plane of PbO_2, deposited on the surface of Bi_2WO_6 in the 2.5 mol%-$FeVO_4/Bi_2WO_6$ photocatalyst. In contrast, Ag nanoparticles with a lattice spacing of 0.235 and 0.200 nm, corresponding to the (111) and (200) planes of Ag, deposited on the surface of $FeVO_4$ in the 2.5 mol%-$FeVO_4/Bi_2WO_6$ photocatalyst. These results suggest that photogenerated electrons accumulated on the surface of $FeVO_4$ and holes accumulated on the surface of Bi_2WO_6 in the $FeVO_4/Bi_2WO_6$ heterojunction, confirming the Z-scheme charge-transfer process in the $FeVO_4/Bi_2WO_6$ heterojunction.

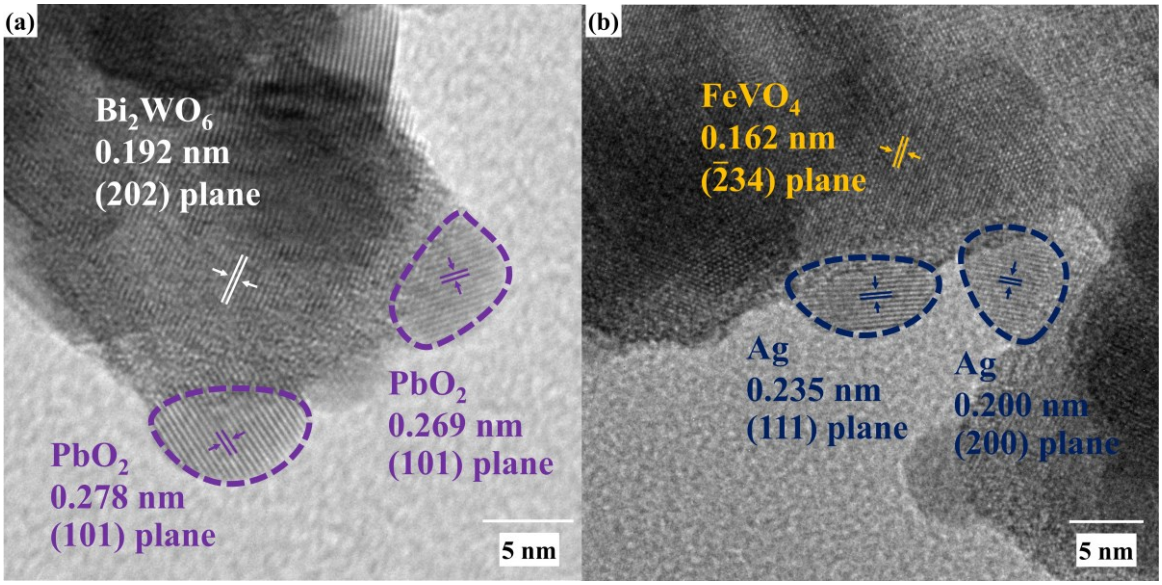

Fig. 17. HRTEM images of (a) PbO_2 nanoparticles deposited on the surface of the Bi_2WO_6 particle and (b) Ag nanoparticles deposited on the surface of $FeVO_4$ in the 2.5 mol%-$FeVO_4/Bi_2WO_6$ nanocomposite.

4. Conclusion

A series of $FeVO_4/Bi_2WO_6$ nanocomposites with different $FeVO_4$ contents (1.25, 2.5, 5, and 10 mol%) were successfully fabricated **via a microwave-assisted calcination process, followed by wet impregnation.** The $FeVO_4/Bi_2WO_6$ nanocomposite with 2.5 mol% of $FeVO_4$

exhibited the greatest photodegradation efficiency for BPA and MB, high recyclability, and stability. **This photocatalyst exhibited different selectivities for organic dye degradation, corresponding to the types and chemical structures of the dyes and the surface charge of the photocatalyst. A comprehensive analysis of scavenging experiments, electron spin resonance technique, nitroblue tetrazolium transformation method, terephthalic acid photoluminescence probing technique, and oxidation of *o*-tolidine by H_2O_2 revealed that •OH, •O_2^-, and e^- were the primary reactive species involved in photodegradation and h^+ was the minor reactive specie.** Its enhanced efficacy was ascribed to the extended visible light absorption and highly efficient generation, separation, and migration of photogenerated charge carriers through interfacial contact in the direct Z-scheme $FeVO_4/Bi_2WO_6$ heterojunction. **This system provided strong reducing ability** to the photogenerated electrons to reduce O_2 to •O_2^- radicals and further produce H_2O_2 and •OH reactive species via a multielectron oxygen reduction process. This heterojunction photocatalyst could be successfully utilized for wastewater remediation under visible-light irradiation with high stability. Further, magnetic properties of the $FeVO_4/Bi_2WO_6$ heterojunction photocatalyst, and the reduction of Cr(VI) ions with coexisting organic pollutant systems will be investigated in future experiments to extend the potential applications of this photocatalyst in the environmental purification field.

Acknowledgements

This project is funded by National Research Council of Thailand (NRCT) and Chiang Mai University : N42A650311. This research project was also supported by Fundamental Fund 2023, Chiang Mai University. T. Luangwanta would like to thank the Institute for the Promotion of Teaching Science and Technology (IPST).

Credit authorship contribution statement

Tawanwit Luangwanta: Methodology; Formal analysis; Investigation; Visualization; Writing – Original draft. **Auttaphon Chachvalvutikul:** Methodology; Investigation; Formal analysis. **Sulawan Kaowphong:** Conceptualization; Methodology; Validation; Investigation; Resources; Writing – Original draft; Writing – review & editing; Visualization; Supervision; Project administration; Funding acquisition.

Conflicts of Interests

The authors declare that there are no conflicts of interest.

References

[1] A.G. Ramu, D. Choi, Highly efficient and simultaneous catalytic reduction of multiple toxic dyes and nitrophenols waste water using highly active bimetallic PdO–NiO nanocomposite, Sci. Rep. 11 (2021) 1–13. https://doi.org/10.1038/s41598-021-01989-7.

[2] H. Liu, J. Liang, S. Fu, L. Li, J. Cui, P. Gao, F. Zhao, J. Zhou, N doped carbon quantum dots modified defect-rich g-C_3N_4 for enhanced photocatalytic combined pollutions degradation and hydrogen evolution, Colloids Surfaces A Physicochem. Eng. Asp. 591 (2020). https://doi.org/10.1016/j.colsurfa.2020.124552.

[3] Y. Cong, Y. Ji, Y. Ge, H. Jin, Y. Zhang, Q. Wang, Fabrication of 3D Bi_2O_3-BiOI heterojunction by a simple dipping method: Highly enhanced visible-light photoelectrocatalytic activity, Chem. Eng. J. 307 (2017) 572–582. https://doi.org/10.1016/j.cej.2016.08.114.

[4] S. Li, M. Cai, C. Wang, Y. Liu, Ta_3N_5/CdS core–shell S-scheme heterojunction nanofibers for efficient photocatalytic removal of antibiotic tetracycline and

Cr(VI): performance and mechanism insights, Adv. Fiber Mater. 5 (2023) 994–1007. https://doi.org/10.1007/s42765-022-00253-5.

[5] M. Cai, Y. Liu, C. Wang, W. Lin, S. Li, Novel $Cd_{0.5}Zn_{0.5}S/Bi_2MoO_6$ S-scheme heterojunction for boosting the photodegradation of antibiotic enrofloxacin: Degradation pathway, mechanism and toxicity assessment, Sep. Purif. Technol. 304 (2023) 122401. https://doi.org/https://doi.org/10.1016/j.seppur.2022.122401.

[6] H. Jiang, J. He, C. Deng, X. Hong, B. Liang, Advances in Bi_2WO_6-based photocatalysts for degradation of organic pollutants, Molecules. 27 (2022) 8698. https://doi.org/10.3390/molecules27248698.

[7] H. Zhao, F. Tian, R. Wang, R. Chen, A review on bismuth-related nanomaterials for photocatalysis, Rev. Adv. Sci. Eng. 3 (2014) 3–27. https://doi.org/10.1166/rase.2014.1050.

[8] V. Dutta, A. Chauhan, R. Verma, C. Gopalkrishnan, V.-H. Nguyen, Recent trends in Bi-based nanomaterials: challenges, fabrication, enhancement techniques, and environmental applications., Beilstein J. Nanotechnol. 13 (2022) 1316–1336. https://doi.org/10.3762/bjnano.13.109.

[9] P. Chen, H. Liu, W. Cui, S.C. Lee, L. Wang, F. Dong, Bi-based photocatalysts for light-driven environmental and energy applications: Structural tuning, reaction mechanisms, and challenges , EcoMat. 2 (2020) 1–31. https://doi.org/10.1002/eom2.12047.

[10] D. Saha, E.D. Bøjesen, A.H. Mamakhel, B.B. Iversen, Why does Bi_2WO_6 visible-light photocatalyst always form as nanoplatelets?, Inorg. Chem. 59 (2020) 9364–9373. https://doi.org/10.1021/acs.inorgchem.0c01249.

[11] K. Lai, Y. Zhu, J. Lu, Y. Dai, B. Huang, N- and Mo-doping Bi_2WO_6 in photocatalytic water splitting, Comput. Mater. Sci. 67 (2013) 88–92. https://doi.org/10.1016/j.commatsci.2012.08.024.

[12] Z. Zhu, S. Wan, Y. Zhao, Y. Qin, X. Ge, Q. Zhong, Y. Bu, Recent progress in Bi_2WO_6-based photocatalysts for clean energy and environmental remediation: Competitiveness, challenges, and future perspectives , Nano Sel. 2 (2021) 187–215. https://doi.org/10.1002/nano.202000127.

[13] S. Fu, W. Yuan, X. Liu, Y. Yan, H. Liu, L. Li, F. Zhao, J. Zhou, A novel 0D/2D WS_2/BiOBr heterostructure with rich oxygen vacancies for enhanced broad-spectrum photocatalytic performance, J. Colloid Interface Sci. 569 (2020) 150–163. https://doi.org/10.1016/j.jcis.2020.02.077.

[14] L. Li, Y. Yan, H. Liu, J. Du, S. Fu, F. Zhao, S.M. Xu, J. Zhou, Hollow core/shell β-Bi_2O_3@WS_2 p-n heterojunction for efficient photocatalytic degradation of fluoroquinolones: A theoretical and experimental study, Inorg. Chem. Front. 7 (2020) 1374–1385. https://doi.org/10.1039/c9qi01594a.

[15] H. Liu, J. Liang, L. shao, J. Du, Q. Gao, S. Fu, L. Li, M. Hu, F. Zhao, J. Zhou, Promoting charge separation in dual defect mediated Z-scheme MoS_2/g-C_3N_4 photocatalysts for enhanced photocatalytic degradation activity: synergistic effect insight, Colloids Surfaces A Physicochem. Eng. Asp. 594 (2020). https://doi.org/10.1016/j.colsurfa.2020.124668.

[16] A. Chachvalvutikul, T. Luangwanta, S. Pattisson, G.J. Hutchings, S. Kaowphong, Enhanced photocatalytic degradation of organic pollutants and hydrogen production by a visible light–responsive Bi_2WO_6/$ZnIn_2S_4$ heterojunction, Appl. Surf. Sci. 544 (2020) 148885. https://doi.org/10.1016/j.apsusc.2020.148885.

[17] S. Li, C. Wang, Y. Liu, Y. Liu, M. Cai, W. Zhao, X. Duan, S-scheme MIL-101(Fe) octahedrons modified Bi_2WO_6 microspheres for photocatalytic decontamination of Cr(VI) and tetracycline hydrochloride: Synergistic insights, reaction pathways, and toxicity analysis, Chem. Eng. J. 455 (2023) 140943.

https://doi.org/https://doi.org/10.1016/j.cej.2022.140943.

[18] Y. Yang, M. Xu, L. Ai, N. Guo, C. Leng, C. Tan, M. Lu, L. Wang, L. Huang, D. Jia, In situ growth of flower sphere Bi_2WO_6/Bi-MOF heterojunction with enhanced photocatalytic degradation of pollutants: DFT calculation and mechanism, J. Environ. Chem. Eng. 11 (2023) 109873. https://doi.org/https://doi.org/10.1016/j.jece.2023.109873.

[19] B. Miao, Y. Chu, X. Zheng, H. Su, Sb_2WO_6/Bi_2WO_6 composite photocatalyst prepared by one-step hydrothermal method: Simple synthesis and excellent visible-light photocatalytic performance, Mater. Sci. Semicond. Process. 125 (2021) 105636. https://doi.org/10.1016/j.mssp.2020.105636.

[20] R. Wang, M. Xu, J. Xie, S. Ye, X. Song, A spherical TiO_2-Bi_2WO_6 composite photocatalyst for visible-light photocatalytic degradation of ethylene, Colloids Surfaces A Physicochem. Eng. Asp. 602 (2020) 125048. https://doi.org/10.1016/j.colsurfa.2020.125048.

[21] T. Xie, Y. Liu, H. Wang, Z. Wu, Synthesis of α-Fe_2O_3/Bi_2WO_6 layered heterojunctions by in situ growth strategy with enhanced visible-light photocatalytic activity, Sci. Rep. 9 (2019) 1–12. https://doi.org/10.1038/s41598-019-43917-w.

[22] S. Li, M. Cai, Y. Liu, C. Wang, R. Yan, X. Chen, Constructing $Cd_{0.5}Zn_{0.5}S$/Bi_2WO_6 S-scheme heterojunction for boosted photocatalytic antibiotic oxidation and Cr(VI) reduction, Adv. Powder Mater. 2 (2023) 100073. https://doi.org/10.1016/j.apmate.2022.100073.

[23] M. Cai, C. Wang, Y. Liu, R. Yan, S. Li, Boosted photocatalytic antibiotic degradation performance of $Cd_{0.5}Zn_{0.5}S$/carbon dots/Bi_2WO_6 S-scheme heterojunction with carbon dots as the electron bridge, Sep. Purif. Technol. 300 (2022) 121892. https://doi.org/https://doi.org/10.1016/j.seppur.2022.121892.

[24] S. Li, M. Cai, Y. Liu, C. Wang, K. Lv, X. Chen, S-Scheme photocatalyst TaON/Bi_2WO_6 nanofibers with oxygen vacancies for efficient abatement of antibiotics and Cr(VI): Intermediate eco-toxicity analysis and mechanistic insights, Chinese J. Catal. 43 (2022) 2652–2664. https://doi.org/https://doi.org/10.1016/S1872-2067(22)64106-8.

[25] Q. Zhang, Y. Zhu, L. Yu, X. Dong, Y. Wu, B. Yang, Q. Xu, Preparation of a visible light catalyst of novel Bi_2WO_6 loaded Ag_3PO_4 heterojunction and its efficient removal of toluene, Environ. Pollut. Bioavailab. 34 (2022) 527–536. https://doi.org/10.1080/26395940.2022.2146000.

[26] H. Wang, L. Zhang, Z. Chen, J. Hu, S. Li, Z. Wang, J. Liu, X. Wang, Semiconductor heterojunction photocatalysts: Design, construction, and photocatalytic performances, Chem. Soc. Rev. 43 (2014) 5234–5244. https://doi.org/10.1039/c4cs00126e.

[27] Y. Li, Z. Zeng, Y. Chen, Y. Zhang, W. Wang, X. Xu, M. Du, Z. Li, Z. Zou, $FeVO_4$ nanowires for efficient photocatalytic CO_2 reduction, Catal. Sci. Technol. 12 (2022) 3289–3294. https://doi.org/10.1039/D2CY00324D.

[28] M.M. Sajid, N.A. Shad, Y. Javed, S.B. Khan, Z. Imran, S. Hassan, Z. Hussain, Z. Zhang, N. Amin, Fast surface charge transfer with reduced band gap energy of $FeVO_4$/graphene nanocomposite and study of its electrochemical property and enhanced photocatalytic activity, Arab. J. Sci. Eng. 44 (2019) 6659–6667. https://doi.org/10.1007/s13369-019-03927-2.

[29] B. Ozturk, G.S. Pozan Soylu, Synthesis of surfactant-assisted $FeVO_4$ nanostructure: characterization and photocatalytic degradation of phenol, J. Mol. Catal. A Chem. 398 (2015) 65–71. https://doi.org/10.1016/j.molcata.2014.11.013.

[30] S.J. Hu, J. Yang, X.H. Liao, Highly efficient degradation of methylene blue on microwave synthesized $FeVO_4$ nanoparticles photocatalysts under visible-light

irradiation, Appl. Mech. Mater. 372 (2013) 153–157. https://doi.org/10.4028/www.scientific.net/AMM.372.153.

[31] Y. Li, S. Chen, A. Xu, F. Ma, F. Chen, W. Lu, Research on the nanocrystal FeV_xO_y catalysts for new reaction from propane to propylene and CO, Appl. Surf. Sci. 320 (2014) 552–557. https://doi.org/10.1016/j.apsusc.2014.09.126.

[32] A. Chachvalvutikul, J. Jakmunee, S. Thongtem, S. Kittiwachana, S. Kaowphong, Novel $FeVO_4/Bi_7O_9I_3$ nanocomposite with enhanced photocatalytic dye degradation and photoelectrochemical properties, Appl. Surf. Sci. 475 (2019) 175–184. https://doi.org/10.1016/j.apsusc.2018.12.214.

[33] A. Chachvalvutikul, S. Kaowphong, Direct Z-scheme $FeVO_4$/BiOCl heterojunction as a highly efficient visible-light-driven photocatalyst for photocatalytic dye degradation and Cr(VI) reduction, Nanotechnology. 31 (2020). https://doi.org/10.1088/1361-6528/ab61d1.

[34] S.K. Tawanwit Luangwanta, Auttaphon Chachvalvutikul, Facile synthesis and enhanced photocatalytic activity of a novel $FeVO_4/Bi_4O_5Br_2$ heterojunction photocatalyst through step-scheme charge transfer mechanism, Colloids Surfaces A Physicochem. Eng. Asp. 627 (2021) 127217. https://doi.org/10.1016/j.colsurfa.2021.127217.

[35] A. Chachvalvutikul, T. Luangwanta, S. Kaowphong, Double Z-scheme $FeVO_4/Bi_4O_5Br_2$/BiOBr ternary heterojunction photocatalyst for simultaneous photocatalytic removal of hexavalent chromium and rhodamine B, J. Colloid Interface Sci. 603 (2021) 738–757. https://doi.org/10.1016/j.jcis.2021.06.124.

[36] Y.J. Zhu, F. Chen, Microwave-assisted preparation of inorganic nanostructures in liquid phase, Chem. Rev. 114 (2014) 6462–6555. https://doi.org/10.1021/cr400366s.

[37] N. Hoang Lam, H.T. Ma, M.J.K. Bashir, G. Eppe, P. Avti, T.T. Nguyen, Removal of phosphate from wastewater using coal slag, Int. J. Environ. Anal. Chem. 101 (2021)

2668–2678. https://doi.org/10.1080/03067319.2019.1708907.

[38] Y. Huang, S. Kang, Y. Yang, H. Qin, Z. Ni, S. Yang, X. Li, Facile synthesis of Bi/Bi_2WO_6 nanocomposite with enhanced photocatalytic activity under visible light, Appl. Catal. B Environ. 196 (2016) 89–99. https://doi.org/10.1016/j.apcatb.2016.05.022.

[39] X. Huang, M. Li, Y. Guo, L. Li, Y. Wu, Hollow nest-like Bi/Bi_2WO_6 photocatalyst with coupled active effects of SPR and defective oxygen, J. Mater. Sci. Mater. Electron. 33 (2022) 19447–19461. https://doi.org/10.1007/s10854-022-08781-x.

[40] X. Meng, Z. Zhang, Facile synthesis of $BiOBr/Bi_2WO_6$ heterojunction semiconductors with high visible-light-driven photocatalytic activity, J. Photochem. Photobiol. A Chem. 310 (2015) 33–44. https://doi.org/https://doi.org/10.1016/j.jphotochem.2015.04.024.

[41] J. Ren, T. Hu, Q. Gong, Q. Wang, B. Sun, T. Gao, P. Cao, G. Zhou, Spherical $Bi_2WO_6/Bi_2S_3/MoS_2$ n-p heterojunction with excellent visible-light photocatalytic reduction Cr(VI) activity, Nanomaterials. 10 (2020). https://doi.org/10.3390/nano10091813.

[42] Y. Huang, S. Kou, X. Zhang, L. Wang, P. Lu, D. Zhang, Facile fabrication of Z-scheme Bi_2WO_6/WO_3 composites for efficient photodegradation of bisphenol a with peroxymonosulfate activation, Nanomaterials. 10 (2020). https://doi.org/10.3390/nano10040724.

[43] K. Saravanakumar, V. Maheskumar, Y. Yea, Y. Yoon, V. Muthuraj, C.M. Park, 2D/2D nitrogen-rich graphitic carbon nitride coupled Bi_2WO_6 S-scheme heterojunction for boosting photodegradation of tetracycline: Influencing factors, intermediates, and insights into the mechanism, Compos. Part B Eng. 234 (2022) 109726. https://doi.org/10.1016/j.compositesb.2022.109726.

[44] J. Jia, P. Xue, R. Wang, X. Bai, X. Hu, J. Fan, E. Liu, The Bi/Bi_2WO_6 heterojunction

with stable interface contact and enhanced visible-light photocatalytic activity for phenol and Cr(VI) removal, J. Chem. Technol. Biotechnol. 93 (2018) 2988–2999. https://doi.org/10.1002/jctb.5657.

[45] P. Du, Y. Zhu, J. Zhang, D. Xu, W. Peng, G. Zhang, F. Zhang, X. Fan, Metallic 1T phase MoS_2 nanosheets as a highly efficient co-catalyst for the photocatalytic hydrogen evolution of CdS nanorods, RSC Adv. 6 (2016) 74394–74399. https://doi.org/10.1039/c6ra10170d.

[46] S. Li, R. Yan, M. Cai, W. Jiang, M. Zhang, X. Li, Enhanced antibiotic degradation performance of $Cd_{0.5}Zn_{0.5}S/Bi_2MoO_6$ S-scheme photocatalyst by carbon dot modification, J. Mater. Sci. Technol. 164 (2023) 59–67. https://doi.org/10.1016/j.jmst.2023.05.009.

[47] C. Wang, R. Yan, M. Cai, Y. Liu, S. Li, A novel organic/inorganic S-scheme heterostructure of TCPP/$Bi_{12}O_{17}Cl_2$ for boosting photodegradation of tetracycline hydrochloride: Kinetic, degradation mechanism, and toxic assessment, Appl. Surf. Sci. 610 (2023) 155346. https://doi.org/https://doi.org/10.1016/j.apsusc.2022.155346.

[48] H. Hamad, M.M. Elsenety, W. Sadik, A. Ghaffar, E. Demerdash, The superior photocatalytic performance and DFT insights of S-scheme CuO@TiO_2 heterojunction composites for simultaneous degradation of organics, Sci. Rep. (2022) 1–20. https://doi.org/10.1038/s41598-022-05981-7.

[49] V. Shivani, S. Harish, J. Archana, M. Navaneethan, S. Ponnusamy, Y. Hayakawa, Highly efficient 3-D hierarchical Bi_2WO_6 catalyst for environmental remediation, Appl. Surf. Sci. 488 (2019) 696–706. https://doi.org/10.1016/j.apsusc.2019.05.072.

[50] W.C. Kee, Y.S. Wong, S.A. Ong, N.A. Lutpi, S.T. Sam, A. Chai, K.M. Eng, Photocatalytic degradation of sugarcane vinasse using ZnO photocatalyst: operating

parameters, kinetic studies, phytotoxicity assessments, and reusability, Int. J. Environ. Res. 16 (2022) 1–13. https://doi.org/10.1007/s41742-021-00382-6.

[51] C.C. Chen, C.S. Lu, H.J. Fan, W.H. Chung, J.L. Jan, H. De Lin, W.Y. Lin, Photocatalyzed N-de-ethylation and degradation of brilliant green in TiO_2 dispersions under UV irradiation, Desalination. 219 (2008) 89–100. https://doi.org/10.1016/j.desal.2007.05.009.

[52] S. Xia, L. Zhang, G. Pan, P. Qian, Z. Ni, Photocatalytic degradation of methylene blue with a nanocomposite system: synthesis, photocatalysis and degradation pathways, Phys. Chem. Chem. Phys. 17 (2015) 5345–5351. https://doi.org/10.1039/C4CP03877K.

[53] X.Q. Wang, S.F. Han, Q.W. Zhang, N. Zhang, D.D. Zhao, Photocatalytic oxidation degradation mechanism study of methylene blue dye waste water with GR/iTO_2, MATEC Web Conf. 238 (2018). https://doi.org/10.1051/matecconf/201823803006.

[54] A. Houas, H. Lachheb, M. Ksibi, E. Elaloui, C. Guillard, J.M. Herrmann, Photocatalytic degradation pathway of methylene blue in water, Appl. Catal. B Environ. 31 (2001) 145–157. https://doi.org/10.1016/S0926-3373(00)00276-9.

[55] Y. Wang, D. Han, Z. Wang, F. Gu, Efficient photocatalytic degradation of tetracycline under visible light by an all-solid-state Z-scheme Ag_3PO_4/MIL-101(Cr) heterostructure with metallic Ag as a charge transmission bridge, ACS Appl. Mater. Interfaces. 101 (2023). https://doi.org/10.1021/acsami.3c01255.

[56] A. Chachvalvutikul, T. Luangwanta, B. Inceesungvorn, S. Kaowphong, Bismuth-rich oxyhalide ($Bi_7O_9I_3$–$Bi_4O_5Br_2$) solid-solution photocatalysts for the degradation of phenolic compounds under visible light, J. Colloid Interface Sci. 641 (2023) 595–609. https://doi.org/10.1016/j.jcis.2023.03.063.

[57] Y. Nosaka, A.Y. Nosaka, Generation and detection of reactive oxygen species in photocatalysis, Chem. Rev. 117 (2017) 11302–11336.

https://doi.org/10.1021/acs.chemrev.7b00161.

[58] W. Bin Zhang, X. Xiao, Q.F. Wu, Q. Fan, S. Chen, W.X. Yang, F.C. Zhang, Facile synthesis of novel Mn-doped $Bi_4O_5Br_2$ for enhanced photocatalytic NO removal activity, J. Alloys Compd. 826 (2020) 154204. https://doi.org/10.1016/j.jallcom.2020.154204.

[59] X. Zhao, Y. You, S. Huang, Y. Wu, Y. Ma, G. Zhang, Z. Zhang, Z-scheme photocatalytic production of hydrogen peroxide over $Bi_4O_5Br_2$/g-C_3N_4 heterostructure under visible light, Appl. Catal. B Environ. 278 (2020) 119251. https://doi.org/10.1016/j.apcatb.2020.119251.

[60] L. Wang, S. Cao, K. Guo, Z. Wu, Z. Ma, L. Piao, Simultaneous hydrogen and peroxide production by photocatalytic water splitting, Chinese J. Catal. 40 (2019) 470–475. https://doi.org/10.1016/s1872-2067(19)63274-2.

[61] J. Liu, Y. Zhang, L. Lu, G. Wu, W. Chen, Self-regenerated solar-driven photocatalytic water-splitting by urea derived graphitic carbon nitride with platinum nanoparticles, Chem. Commun. 48 (2012) 8826–8828. https://doi.org/10.1039/c2cc33644h.